

REPORT DOCUMENTATION PAGE				Form Approved OMB No. 0704-0188	
The public reporting burden for this collection of information is estimated to average 1 hour per response, including the time for reviewing instructions, searching existing data sources, gathering and maintaining the data needed, and completing and reviewing the collection of information. Send comments regarding this burden estimate or any other aspect of this collection of information, including suggestions for reducing the burden, to Department of Defense, Washington Headquarters Services, Directorate for Information Operations and Reports (0704-0188), 1215 Jefferson Davis Highway, Suite 1204, Arlington, VA 22202-4302. Respondents should be aware that notwithstanding any other provision of law, no person shall be subject to any penalty for failing to comply with a collection of information if it does not display a currently valid OMB control number.					
PLEASE DO NOT RETURN YOUR FORM TO THE ABOVE ADDRESS.					
1. REPORT DATE (DD-MM-YYYY) 20/Aug/2001		2. REPORT TYPE THESIS		3. DATES COVERED (From - To)	
4. TITLE AND SUBTITLE A COMBINATION OF RAO-WILTON-GLISSON AND ASYMPTOTIC PHASE BASIS FUNCTIONS TO SOLVE THE ELECTRIC AND MAGNETIC FIELD INTEGRAL EQUATIONS				5a. CONTRACT NUMBER	
				5b. GRANT NUMBER	
				5c. PROGRAM ELEMENT NUMBER	
				5d. PROJECT NUMBER	
6. AUTHOR(S) 2D LT GULICK JOHN R				5e. TASK NUMBER	
				5f. WORK UNIT NUMBER	
7. PERFORMING ORGANIZATION NAME(S) AND ADDRESS(ES) MICHIGAN STATE UNIVERSITY				8. PERFORMING ORGANIZATION REPORT NUMBER CI01-201	
9. SPONSORING/MONITORING AGENCY NAME(S) AND ADDRESS(ES) THE DEPARTMENT OF THE AIR FORCE AFIT/CIA, BLDG 125 2950 P STREET WPAFB OH 45433				10. SPONSOR/MONITOR'S ACRONYM(S)	
				11. SPONSOR/MONITOR'S REPORT NUMBER(S)	
12. DISTRIBUTION/AVAILABILITY STATEMENT Unlimited distribution In Accordance With AFI 35-205/AFIT Sup 1					
13. SUPPLEMENTARY NOTES					
20010904 045					
14. ABSTRACT					
15. SUBJECT TERMS					
16. SECURITY CLASSIFICATION OF:			17. LIMITATION OF ABSTRACT	18. NUMBER OF PAGES 62	19a. NAME OF RESPONSIBLE PERSON
a. REPORT	b. ABSTRACT	c. THIS PAGE			19b. TELEPHONE NUMBER (Include area code)

## ABSTRACT

### A COMBINATION OF RAO-WILTON-GLISSON AND ASYMPTOTIC PHASE BASIS FUNCTIONS TO SOLVE THE ELECTRIC AND MAGNETIC FIELD INTEGRAL EQUATIONS

By

John Robert Gulick

Using the method of moments to solve the electric and magnetic field integral equations for the currents on a PEC surface requires a large number of unknowns to capture the current's rapid spatial variation across the surface. Rao-Wilton-Glisson (RWG) vector basis functions [1] have been successfully used for the past twenty years [1, 2, 3,...]. Unfortunately, the required number of unknowns is on the order of 100 per square wavelength making electrically large problems impractical. For large smooth objects, the rapid spatial variation in the current is due to phase variations rather than magnitude variations. Thus, using asymptotic phase (AP) basis functions can drastically reduce the number of unknowns [3] for large, smooth metallic bodies. The AP basis function incorporates the anticipated phase, hence represents a more efficient basis function for a large class of problems. However, using RWG basis functions for monostatic calculations is more efficient since the matrix entries need not be recomputed for each new incidence angle, as is the case for an AP expansion. One can combine the methods; selecting RWG or AP basis functions for a given geometry based on an element's location within the geometry. This allows the relaxation of mesh density in smooth flat regions not near the discontinuities resulting in a significant reduction of unknowns. This research shows that combining functions is highly efficient and the effectiveness of this method depends on the geometry of application.

A COMBINATION OF RAO-WILTON-GLISSON AND ASYMPTOTIC PHASE  
BASIS FUNCTIONS TO SOLVE THE ELECTRIC AND MAGNETIC FIELD  
INTEGRAL EQUATIONS

By

John Robert Gulick

A THESIS

Submitted to  
Michigan State University  
in partial fulfillment of the requirements  
for the degree of

MASTER OF SCIENCE

Department of Electrical and Computer Engineering

2001

**THE VIEWS EXPRESSED IN THIS ARTICLE  
ARE THOSE OF THE AUTHOR AND DO NOT  
REFLECT THE OFFICIAL POLICY OR  
POSITION OF THE UNITED STATES,  
DEPARTMENT OF DEFENSE, OR THE U.S.  
GOVERNMENT**

Integrity, Ambition, Knowledge, Communication, Excellence, Service, Love.

"Science serves humanity only when it is joined to conscience."

-Pope John Paul II, Padua, Italy, 1992, to International Conference on Space Research

## ACKNOWLEDGEMENTS

Several people have significantly impacted and/or assisted me in this journey. To them, I owe deep gratitude, that which is insufficiently accomplished by mere prose.

Great appreciation is given to Pamela Haddad who provided her method of moments code for this research.

Dennis Nyquist, Ed Rothwell, and David Infante have inspired my interest and career by opening my eyes to the intriguing mathematical world of electromagnetics. Their thirst for knowledge, integrity, and sense of humor set a high standard for engineers, mathematicians, professors, and professionals.

I thank Leo C. Kempel, whose vast knowledge and energy inspired and continually supported me through graduate school, for his concern, humor, and high expectations.

Col (USAF Ret) Gale Larson has guided me as an officer mentor, showing me the value of depth and breadth of knowledge, excellence, integrity, and service.

Without the continued love and support of my beautiful wife all potential would forever remain unfulfilled.

# TABLE OF CONTENTS

List of Tables .....	vii
List of Figures .....	viii
Key to Abbreviations .....	x
Introduction.....	1
Chapter 1: Integral Equations .....	2
1. Configuration .....	2
2. Electric Field Integral Equation.....	4
3. Magnetic Field Integral Equation .....	6
4. Combined Field Integral Equation (CFIE) .....	7
5. Summary.....	8
Chapter 2: Method of Moments .....	9
1. Method of Moments.....	9
2. Expansion and Testing Functions .....	10
3. Electric Field Integral Equation Method Of Moments .....	11
4. Magnetic Field Integral Equation Method of Moments .....	17
Chapter 3: Basis Function Specification.....	19
1. Sub-domain Vector Basis Functions.....	19
2. Impedance Matrix .....	21
3. Singularities .....	24
4. Coding.....	24
Chapter 4: Results .....	25
1. Square Plate .....	25
2. The Kite: Description.....	26
3. The Kite: Results .....	29
Code Validation Case: .....	30
RCS Curve Comparison:.....	31
Selection of the RWG Region Thickness: .....	34
Convergence: .....	35
Mesh Density Analysis: .....	36
4. Extension to the EMCC Mini-Arrow.....	38
Chapter 5: Conclusion.....	40
1. Summary .....	40
Summary of Results from Specific Geometries.....	41
Conclusion .....	42
2. Challenges.....	43

3. Future Work.....	43
Appendix A: Fundamental Theory .....	46
1. Maxwell's Equations .....	46
2. Boundary Conditions .....	51
3. Vector Potentials.....	51
Magnetic Vector Potential: .....	52
Electric Vector Potential: (source free space.).....	53
4. Scalar Green's Function .....	53
Appendix B: Vector Identities .....	56
Appendix C: Inner Kite Vertices .....	57
Appendix D: Additional Kite Separation Comparisons.....	58
Bibliography .....	61



## LIST OF TABLES

Table 4.1: Problem Size .....	30
Table 4.2: Mesh Density Analysis .....	36

## LIST OF FIGURES

Figure 1.1: Configuration .....	3
Figure 2.1: Current on a 4x4 Wavelength Square Plate .....	10
Figure 3.1: Sub-domain Parameters.....	20
Figure 3.2: Local Position in Terms of Global .....	23
Figure 4.1: Sample results for a $4\lambda \times 4\lambda$ plate.....	25
Figure 4.2: Scattering by a $10\lambda \times 10\lambda$ plate.....	26
Figure 4.3: The Kite.....	26
Figure 4.4: Waterline Cut .....	27
Figure 4.5: Over the Top Cut.....	27
Figure 4.6: Kite Mesh .....	28
Figure 4.7: 5 GHz Kite RCS Plot, $d = 1.5$ cm, Density Factor = $12/3$ .....	31
Figure 4.8: 10 GHz Kite RCS Plot, Mesh Density Factor = $12/12$ .....	32
Figure 4.9: 10 GHz Kite, $d = 1.5$ cm, Mesh Density Factor = $12/3$ .....	33
Figure 4.10: 10Ghz Kite RCS Plot, $d = 1.5$ cm, Density Factor = $12/3$ .....	33
Figure 4.11: 10 GHz Kite RCS Plots, $d = 1$ cm, Mesh Density Factor = $12/3$ .....	34
Figure 4.12: 10 GHz Kite RCS, OTT-T Mixed Basis Functions .....	35
Figure 4.13: 10 GHz Kite, $d = 1$ cm, Condition Number vs. Incident Angle.....	36
Figure 4.14: 12 GHz Kite RCS, OTT-T, $d = 1.25$ cm .....	37
Figure 4.15: Condition Number vs. Incident Angle .....	37
Figure 4.16: Mini-arrow scattering at 9 GHz.....	38
Figure 5.1: Graded Mesh on Square Plate vs. Conesphere.....	42

Figure A.1: Position Vectors.....	54
Figure D.1: 10 GHz Kite RCS, AP Basis Functions.....	58
Figure D.2: 10 GHz Kite RCS, Mixed Basis Functions .....	59
Figure D.3: 10 GHz Kite RCS, RWG Basis Functions .....	59

## **KEY TO ABBREVIATIONS**

AP – Asymptotic Phase

CFIE – Combined Field Integral Equation

EFIE – Electrical Field Integral Equation

EMCC – Electromagnetic Code Consortium

GHz – Gigahertz

IE – Integral Equation

MFIE – Magnetic Field Integral Equation

MoM – Method of Moments

OTT-P – Over the top cut, phi polarization

OTT-T – Over the top cut, theta polarization

PEC – Perfect Electric Conductor

RCS – Radar Cross Section

RWG – Rao, Wilton, Glisson

WL-P – Waterline cut, phi polarization

## INTRODUCTION

This thesis presents the theoretical development and numerical solution results for implementing a method of moments solution technique combining Rao-Wilton-Glisson (RWG) basis functions [1] and Asymptotic (AP) basis functions [3] over the same surface. With the intention of broadening the potential audience beyond just the electromagnetics community, included in Appendix A is background material commencing from Maxwell's independent equations. The theoretical development in chapter one continues where Appendix A leaves off and develops the familiar form of the electric and magnetic field integral equations along with a standard method of combining the equations. Chapter two discusses the method of moments technique and introduces the implementation of combined RWG and AP basis and testing functions to derive the impedance matrix for the electric field integral equation (EFIE) and magnetic field integral equation (MFIE). In chapter three, the basis functions are incorporated into the EFIE matrix equation in a manner that can be solved computationally. Chapter 4 presents computational results, comparison, and discussion for implementation of this technique on two square plates, a kite geometry, and the Electromagnetic Code Consortium (EMCC) mini-arrow. The final chapter summarizes the specific knowledge gained from this research.

The research shows that the technique is a more efficient solution method than existing methods for geometries with large, smooth, low curvature regions.

## CHAPTER 1: INTEGRAL EQUATIONS

The first three chapters develop the theory for the problem this research addresses. After discussing the configuration and general problem, chapter one introduces the electric and magnetic field integral equations.

### 1. Configuration

The problem is a traditional scattering problem as shown in figure 1. An arbitrary perfect electrically conducting (PEC) surface is immersed in free space. A known current source creates impressed electric and magnetic fields ( $\mathbf{E}^i$  and  $\mathbf{H}^i$ ). Due to the necessity of matching boundary conditions on the PEC surface, the impressed fields excite a surface

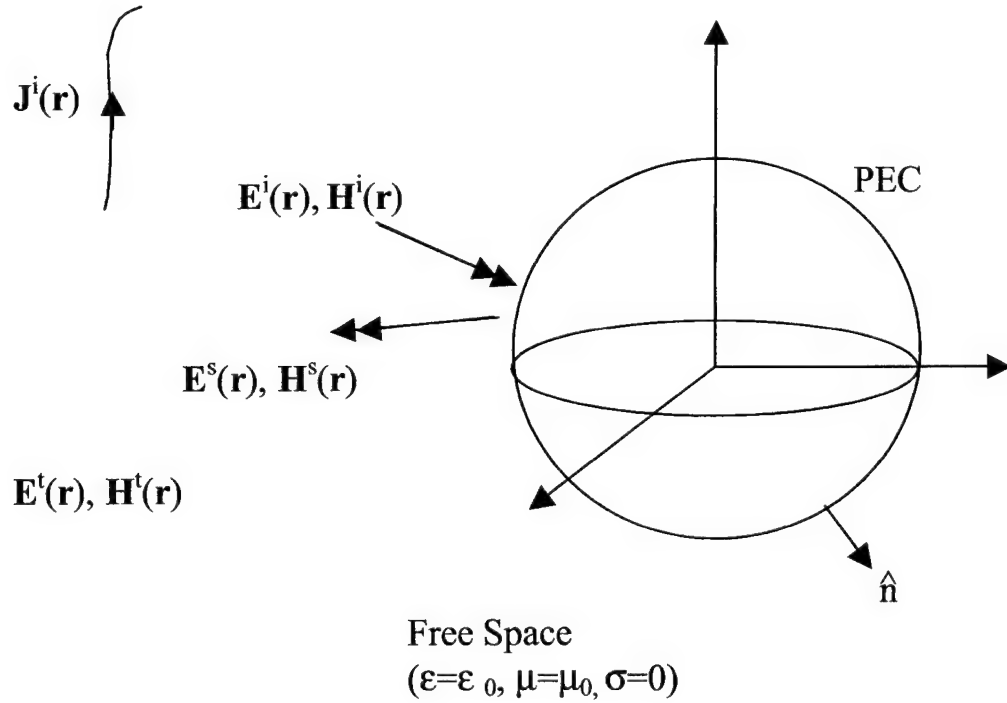


Figure 1.1: Configuration

current  $\mathbf{J}_s$  on the PEC object. The surface current induces scattered electric and magnetic fields ( $\mathbf{E}^s$  and  $\mathbf{H}^s$ ), as required to satisfy the boundary conditions. The total fields in the free space region ( $\mathbf{E}^t$  and  $\mathbf{H}^t$ ) are the sum of the impressed and scattered fields. It is the total fields that must satisfy the boundary conditions on the surface of the PEC object. The following fundamental equations are derived in Appendix A along with the complex transform domain form of Maxwell's equations. Quantities  $\mathbf{E}$ ,  $\mathbf{H}$ ,  $\mathbf{A}$ ,  $\mathbf{J}$ , and  $\Phi$  have suppressed position dependence  $\mathbf{r}$ . Vector  $\mathbf{r}'$  denotes the source position while  $\mathbf{r}$  denotes the position vector to the observation point. Note that the first five equations contain a suppressed  $e^{j\omega t}$  time dependence term.

$$\nabla \times \mathbf{E} = -j\omega\mu\mathbf{H} \quad \dots \text{Faraday's Law} \quad (1.1)$$

$$\nabla \times \mathbf{H} = \mathbf{J}^i + (\sigma + j\omega\epsilon)\mathbf{E} \quad \dots \text{Ampere's Law} \quad (1.2)$$

$$\nabla \cdot \mathbf{E} = \frac{1}{\epsilon} \rho(\mathbf{r}) \quad \dots \text{Gauss' Law} \quad (1.3)$$

$$\nabla \cdot \mathbf{H} = 0 \quad \dots \text{Gauss's Magnetic Law} \quad (1.4)$$

$$\nabla \cdot \mathbf{J} = -j\omega\rho(\mathbf{r}) \quad \dots \text{Continuity Equation} \quad (1.5)$$

$$\Phi_e = \frac{j\omega}{k^2} \nabla \cdot \mathbf{A} \quad \dots \text{Lorentz gauge conditions} \quad (1.6)$$

$$k^2 = \omega^2 \mu\epsilon \quad \dots \text{wave number } k \text{ in free space} \quad (1.7)$$

$$\mu\mathbf{H} = \nabla \times \mathbf{A} \quad \dots \mathbf{H} \text{ in terms of vector potential } \mathbf{A} \quad (1.8)$$

$$\mathbf{E} = -\nabla\Phi_e - j\omega\mathbf{A} \quad \dots \mathbf{E} \text{ in terms of vector potential } \mathbf{A} \quad (1.9)$$

$$\hat{n} \times \mathbf{E}^t = 0 \quad \dots \text{Boundary Conditions describing the} \quad (1.10)$$

$$\hat{n} \times \mathbf{H}^t = \mathbf{J}_s \quad \dots \text{tangential component of the total field.} \quad (1.11)$$

$$\nabla^2 \mathbf{A} + k^2 \mathbf{A} = -\mu\mathbf{J}^i \quad \dots \text{scalar Helmholtz equation} \quad (1.12)$$

$$g(\mathbf{r} | \mathbf{r}') = \frac{1}{4\pi R} e^{-jkR} \quad \dots \text{unbound region Green's function for (1.12)} \quad (1.13)$$

$$\mathbf{A} = \mu \int_s \mathbf{J}(\mathbf{r}') g(\mathbf{r} | \mathbf{r}') ds' \quad \dots \text{a solution to (1.12) in terms of (1.13)} \quad (1.14)$$

Given the impressed current, we know the impressed fields. By enforcing the boundary conditions for the total fields, we can solve for the desired scattered fields. If we can solve for the surface currents, we can then get  $\mathbf{A}$  from (1.14) and find the scattered fields, from (1.6), (1.8), and (1.9). Due to the uniqueness theorem [4], if we find a solution to Maxwell's equations by enforcing all the relevant boundary conditions, the solution is unique.

## 2. Electric Field Integral Equation

Enforcing the boundary condition  $\hat{n} \times \mathbf{E}^t = 0$  at the surface of the PEC object and using subscript t to denote the tangential field components,

$$\mathbf{E}_t^t = \mathbf{E}_t^i + \mathbf{E}_t^s = 0 \Rightarrow \mathbf{E}_t^i = -\mathbf{E}_t^s. \quad (1.15)$$

Writing  $-\mathbf{E}_t^s$  using (1.6), and (1.9),

$$\mathbf{E}_t^s(\mathbf{r}) = \left[ -\nabla \left( \frac{j\omega}{k^2} \nabla \cdot \mathbf{A} \right) - j\omega \mathbf{A} \right]_t = -j\omega \left( \mathbf{A} + \frac{1}{k^2} \nabla \nabla \cdot \mathbf{A} \right)_t. \quad (1.16)$$

Expanding  $\mathbf{A}$  with (1.14) and substituting into (1.16),

$$\mathbf{E}_t^i(\mathbf{r} = \mathbf{r}_s) = j\omega\mu \left( \int_s \mathbf{J}(\mathbf{r}') g(\mathbf{r}_s | \mathbf{r}') ds' + \frac{1}{k^2} \nabla \nabla \cdot \int_s \mathbf{J}(\mathbf{r}') g(\mathbf{r}_s | \mathbf{r}') ds' \right). \quad (1.17)$$

In the second term of the integrand of (1.17), the divergence operator may be taken inside the integration since it operates on observation points while the integration is taken over source points. The notation denoting tangential field components will be suppressed unless required for clarity.

$$\nabla \cdot \int_s [\mathbf{J}(\mathbf{r}') g(\mathbf{r} | \mathbf{r}')] ds' = \int_s \nabla \cdot [\mathbf{J}(\mathbf{r}') g(\mathbf{r} | \mathbf{r}')] ds' \quad (1.18)$$



Using the vector identity  $\nabla \cdot (w\mathbf{V}) = w\nabla \cdot \mathbf{V} + \mathbf{V} \cdot \nabla w$  on the integrand of the right hand side,  $\nabla \cdot [\mathbf{J}(\mathbf{r}')g(\mathbf{r} | \mathbf{r}')] = g(\mathbf{r} | \mathbf{r}')\nabla \cdot \mathbf{J}(\mathbf{r}') + \mathbf{J}(\mathbf{r}') \cdot \nabla g(\mathbf{r} | \mathbf{r}')$ . Since  $\mathbf{J}(\mathbf{r}')$  is a function of primed coordinates and is a constant with respect to the unprimed coordinates, the unprimed derivative of  $\mathbf{J}(\mathbf{r}') = 0 \Rightarrow \nabla \cdot \mathbf{J}(\mathbf{r}') = 0$ . Due to the symmetry of the Green's function,  $\nabla g(\mathbf{r} | \mathbf{r}') = -\nabla' g(\mathbf{r} | \mathbf{r}')$ . Using the same vector identity as above,  $-\mathbf{J}(\mathbf{r}') \cdot \nabla' g(\mathbf{r} | \mathbf{r}') = -\nabla' \cdot [\mathbf{J}(\mathbf{r}')g(\mathbf{r} | \mathbf{r}')] + g(\mathbf{r} | \mathbf{r}')\nabla' \cdot \mathbf{J}(\mathbf{r}')$ . For closed three-dimensional bodies, if we split the volume into two surfaces,  $s_1$  and  $s_2$  along a cut  $c$  with contours  $c_1$  and  $c_2$  respectively and in opposite directions, we can apply a two-dimensional version of the divergence theorem as in [20] on p17.

$$\begin{aligned}
& \int_s \nabla' \cdot [\mathbf{J}(\mathbf{r}')g(\mathbf{r} | \mathbf{r}')] ds' \\
&= \int_{s_1} \nabla' \cdot [\mathbf{J}(\mathbf{r}')g(\mathbf{r} | \mathbf{r}')] ds' + \int_{s_2} \nabla' \cdot [\mathbf{J}(\mathbf{r}')g(\mathbf{r} | \mathbf{r}')] ds' \\
&= \oint_{c_1} \hat{n}_l \cdot \mathbf{J}(\mathbf{r}')g(\mathbf{r} | \mathbf{r}') dl + \oint_{c_2} \hat{n}_l \cdot \mathbf{J}(\mathbf{r}')g(\mathbf{r} | \mathbf{r}') dl \\
&= 0.
\end{aligned} \tag{1.19}$$

For open surfaces, this identity follows by straightforward application of the divergence theorem. Therefore,

$$\nabla \cdot \int_s [\mathbf{J}(\mathbf{r}')g(\mathbf{r} | \mathbf{r}')] ds' = \int_s g(\mathbf{r} | \mathbf{r}') \nabla' \cdot \mathbf{J}(\mathbf{r}') ds'. \tag{1.20}$$

The electric field integral equation (EFIE) is by substitution of (1.20) into (1.17),

$$\mathbf{E}_t^i(\mathbf{r} = \mathbf{r}_s) = j\omega\mu \left( \int_s \mathbf{J}(\mathbf{r}')g(\mathbf{r}_s | \mathbf{r}') ds' + \frac{1}{k^2} \nabla \int_s g(\mathbf{r}_s | \mathbf{r}') \nabla' \cdot \mathbf{J}(\mathbf{r}') ds' \right). \tag{1.21}$$

### 3. Magnetic Field Integral Equation

The tangential magnetic field is discontinuous by the amount of current density induced on the surface of the PEC;  $\hat{n} \times \mathbf{H}^t = \mathbf{J}_s$ ,

$$\mathbf{J}_s(\mathbf{r}') = \hat{n} \times [\mathbf{H}^i(\mathbf{r}') + \mathbf{H}^s(\mathbf{r}')]. \quad (1.22)$$

$\mathbf{H}^s$  may be written in terms of  $\mathbf{A}$  using (1.14),

$$\mathbf{H}^s(\mathbf{r}) = \frac{1}{\mu} \nabla \times \mathbf{A} = \nabla \times \int_s \mathbf{J}_s(\mathbf{r}') g(\mathbf{r} | \mathbf{r}') ds'. \quad (1.23)$$

Due to the physical nature of the problem, we can safely assume uniform convergence of the integrand. Thus, we can interchange the order of integration and differentiation.

Then, rewriting (1.23) using the vector identity  $\nabla \times (\mathbf{V}w) = w\nabla \times \mathbf{V} - \mathbf{V} \times \nabla w$ ,

$$\begin{aligned} \mathbf{H}^s(\mathbf{r}) &= \int_s \nabla \times [\mathbf{J}_s(\mathbf{r}') g(\mathbf{r} | \mathbf{r}')] ds' \\ &= \int_s \{g(\mathbf{r} | \mathbf{r}') \nabla \times \mathbf{J}_s(\mathbf{r}') - \mathbf{J}_s(\mathbf{r}') \times \nabla g(\mathbf{r} | \mathbf{r}')\} ds'. \end{aligned} \quad (1.24)$$

However,  $\nabla \times \mathbf{J}_s(\mathbf{r}') = 0$  since the unprimed derivative of a function of primed coordinates is zero. From the symmetry of the Green's function,  $\nabla g(\mathbf{r} | \mathbf{r}') = -\nabla' g(\mathbf{r} | \mathbf{r}')$ , (1.24) becomes,

$$\mathbf{H}^s(\mathbf{r}) = \int_s \mathbf{J}_s(\mathbf{r}') \times [\nabla' g(\mathbf{r} | \mathbf{r}')] ds'. \quad (1.25)$$

Inserting (1.25) into (1.22),

$$\hat{n} \times \mathbf{H}^i(\mathbf{r}) = \frac{\mathbf{J}_s(\mathbf{r})}{2} - \lim_{r \rightarrow s^+} \left\{ \hat{n} \times \int_s \mathbf{J}_s(\mathbf{r}') \times \nabla' g(\mathbf{r} | \mathbf{r}') ds' \right\} \quad (1.26)$$

where  $r \rightarrow s^+$  indicates that  $s$  is approached from the outside. Due to the discontinuity at the surface, the integral should be taken in the principal value sense [5].

$$\hat{n} \times \mathbf{H}^i(\mathbf{r}) = \frac{\mathbf{J}_s(\mathbf{r})}{2} - \oint_s \hat{n} \times \mathbf{J}_s(\mathbf{r}') \times \nabla' g(\mathbf{r} | \mathbf{r}') ds' \quad (1.27)$$

Equation (1.27) is referred to as the magnetic field integral equation (MFIE), valid for closed surfaces [9].

The EFIE and MFIE are actually integrodifferential equations since the unknown quantity is in the integrand of a differential equation. However, they are commonly referred to as integral equations. In general, they are both classified as inhomogeneous Fredholm equations where the EFIE is of the first kind and the MFIE is of the second kind. For more information on classification, see [10].

#### ***4. Combined Field Integral Equation (CFIE)***

Although either the MFIE or the EFIE is sufficient to finding the scattered fields, a combination can also be used. Using only EFIE or MFIE leads to spurious resonances for closed scattering bodies [5]. These are resolved using a method that introduces a mixing constant  $\alpha \in [0,1]$  to formulate the CFIE, providing stable, unique solutions for all closed scatterers [11,12].

$$\alpha [EFIE] + \frac{1}{jk_o} (\alpha - 1) [MFIE] \quad (1.28)$$

In this implementation,  $\alpha = 1$  reduces to a pure EFIE formulation while  $\alpha = 0$  reduces to a pure MFIE formulation.

## 5. Summary

$$\text{EFIE: } \mathbf{E}_t^i(\mathbf{r}) = j\omega\mu \left( \int_s \mathbf{J}(\mathbf{r}') g(\mathbf{r}_s | \mathbf{r}') ds' + \frac{1}{k^2} \nabla \int_s g(\mathbf{r}_s | \mathbf{r}') \nabla' \cdot \mathbf{J}(\mathbf{r}') ds' \right)$$

$$\text{MFIE: } \hat{n} \times \mathbf{H}^i(\mathbf{r}) = \frac{\mathbf{J}_s(\mathbf{r})}{2} - \oint_s \hat{n} \times \mathbf{J}_s(\mathbf{r}') \times \nabla' g(\mathbf{r} | \mathbf{r}') ds'$$

$$\text{CFIE: } \alpha [EFIE] + \frac{1}{jk_o} (\alpha - 1) [MFIE]$$

None of these integral equations are easy to solve analytically except for a few special circumstances. Numerical techniques such as the method of moments (MoM) can be used to find solutions. When implementing the MoM, one chooses an expansion function set that can accurately represent the anticipated unknown function while minimizing the cost to employ it. The method of moments numerical technique applied to these integral equations is the topic of the next chapter.

## CHAPTER 2: METHOD OF MOMENTS

Numerical techniques, such as the method of moments (MoM), can be used to find solutions to the integral equations developed in the previous chapter. When implementing the MoM, one chooses an expansion function set that can accurately represent the anticipated unknown function while minimizing the cost to employ it. The focal point of this research is on evaluating a potentially improved (good representation of the solution with minimal employment cost) expansion function set for a particular class of problems. This research considers combining two existing sub-domain expansion functions, Rao-Wilton-Glisson and Asymptotic Phase, within the same problem. Chapter 2 discusses the method of moments formulation using both types of expansion functions and develops the impedance matrix for use in a numerical solution.

### *1. Method of Moments*

For a surface, subdivided into a mesh of triangle elements, there are  $N$  edges. The basis functions are associated with the edges of the mesh with support spanning two adjacent triangles. The total surface current is formed by the superposition of the various basis functions. Using the method of moments, we chose a sub-domain expansion function to represent the current across each element. Since there are  $N$  edges, each edge has a different expansion coefficient. We then choose a testing function. Using Galerkin's method, the testing function is selected as the same as the basis function. We expand the current with the expansion function, multiply each term in the integral equation by the testing function, and integrate over the surface.

## 2. Expansion and Testing Functions

Using the method of moments, we approximate the current by a set of expansion (equivalently basis) functions and "test" the integral equation with a testing function. Rao, Wilton, and Glisson developed [1] a sub-domain basis function that can be used to accurately approximate the current over a surface element and also serves as a testing function. Let  $\mathbf{f}(\mathbf{r})$  represent the RWG sub-domain basis function. Since that phase of the incident field is known, we can assume the phase of the surface current should vary spatially approximately as the incident phase varies in regions not near location of rapid curvature change. This is one critical approximation made in the popular asymptotic solution method, the physical optics (PO) method. [6] RWG basis functions, modified by the incident phase term, are Asymptotic Phase (AP) basis functions [6] with  $\mathbf{F}(\mathbf{r}) = \mathbf{f}(\mathbf{r})e^{-j\mathbf{k}^i \cdot \mathbf{r}}$ . Thus, including the incident phase in the basis functions should allow a reduction in the density of the mesh for regions away from discontinuities. Indeed this concept is illustrated in figure 2.1 which compares the variation of the real part of the x-component of the current for standard RWG basis functions and AP basis functions for a four wavelength square plate.

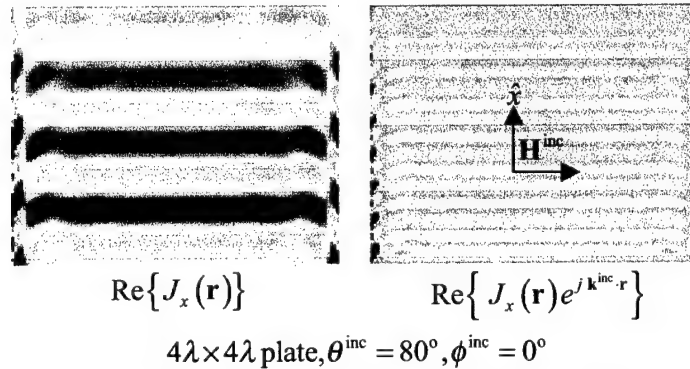


**Figure 2.1:** Current on a 4x4 Wavelength Square Plate

For testing functions,  $\mathbf{f}(\mathbf{r})$ ,  $\mathbf{F}^*(\mathbf{r})$ , and  $\mathbf{F}(\mathbf{r})$  were considered. However, the first two lead to asymmetric matrices while the third choice yields a symmetric matrix as will be shown in the next section. Thus, we will use  $\mathbf{F}(\mathbf{r})$  for both the testing and expansion functions. To allow control over the testing and expansion function for each edge of the mesh independently, we introduce a constant  $\beta_n = 0$  or  $\beta_n = 1$  such that the current expansion is given by

$$\mathbf{J}(\mathbf{r}) = \sum_{n=1}^N J_n \mathbf{F}_n(\mathbf{r}) = \sum_{n=1}^N J_n \mathbf{f}_n(\mathbf{r}) e^{-j\beta_n \hat{\mathbf{k}}^i \cdot \mathbf{r}}. \quad (2.1)$$

The subscript,  $n$ , denotes a specific edge of the mesh. In this representation,  $\beta_n = 1$  means AP function while  $\beta_n = 0$  reduces to the RWG basis function. For the impedance matrix elements where the testing and expansion functions are the same, the implementation of the MOM is termed Galerkin's method. The impedance matrix is derived by testing the EFIE and expanding the unknown current using our flexible (either RWG or AP) basis and testing functions.

### 3. Electric Field Integral Equation Method Of Moments

$$\text{EFIE: } \mathbf{E}_t^i(\mathbf{r}) = j\omega\mu \left( \int_s \mathbf{J}(\mathbf{r}') g(\mathbf{r}_s | \mathbf{r}') ds' + \frac{1}{k^2} \nabla \int_s g(\mathbf{r}_s | \mathbf{r}') \nabla' \cdot \mathbf{J}(\mathbf{r}') ds' \right) \quad (2.2)$$

Assume the medium is *free space*. Let the  $m$  indices denote the testing edge and  $n$  denote the expansion edge. Testing equation (2.2) with  $\mathbf{F}_m(\mathbf{r})$  requires pre-multiplication by  $\mathbf{F}_m(\mathbf{r})$  and integration over the domain of each testing function.

$$\begin{aligned} \int_s \mathbf{F}_m(\mathbf{r}) \cdot \mathbf{E}^i(\mathbf{r}) ds &= j\omega\mu \int_s \int_{s'} \mathbf{F}_m(\mathbf{r}) \cdot \mathbf{J}(\mathbf{r}') g(\mathbf{r}_s | \mathbf{r}') ds' ds \\ &+ \frac{j\omega\mu}{k_o^2} \int_s \mathbf{F}_m(\mathbf{r}) \cdot \nabla \int_{s'} g(\mathbf{r}_s | \mathbf{r}') \nabla' \cdot \mathbf{J}(\mathbf{r}') ds' ds. \end{aligned} \quad (2.3)$$

For notational convenience, define A, B, and C such that (2.3) has the form

$$A = j\omega\mu \left[ B + \frac{1}{k_o^2} C \right].$$

$$A = \int_s \mathbf{F}_m(\mathbf{r}) \cdot \mathbf{E}^i(\mathbf{r}) ds \quad (2.4)$$

$$B = \int_s \int_{s'} \mathbf{F}_m(\mathbf{r}) \cdot \mathbf{J}(\mathbf{r}') g(\mathbf{r}_s | \mathbf{r}') ds' ds \quad (2.5)$$

$$C = \int_s \mathbf{F}_m(\mathbf{r}) \cdot \nabla \int_{s'} g(\mathbf{r}_s | \mathbf{r}') \nabla' \cdot \mathbf{J}(\mathbf{r}') ds' ds \quad (2.6)$$

Manipulating C by first switching the order of integration,

$$C = \int_{s'} \nabla' \cdot \mathbf{J}(\mathbf{r}') \int_s \mathbf{F}_m(\mathbf{r}) \cdot \nabla g(\mathbf{r}_s | \mathbf{r}') ds ds' \quad (2.7)$$

then, using the vector id  $\nabla \cdot (w\mathbf{V}) = w\nabla \cdot \mathbf{V} + \mathbf{V} \cdot \nabla w$  as  $\mathbf{V} \cdot \nabla w = \nabla \cdot \mathbf{V}w - \nabla \cdot (\mathbf{V}w)$ ,

$$C = \int_{s'} \nabla' \cdot \mathbf{J}(\mathbf{r}') \left[ \int_s \nabla \cdot [\mathbf{F}_m(\mathbf{r}) g(\mathbf{r}_s | \mathbf{r}')] ds - \int_s \nabla \cdot \mathbf{F}_m(\mathbf{r}) g(\mathbf{r}_s | \mathbf{r}') ds \right] ds'. \quad (2.8)$$

Using the same technique as in (1.19),

$$\int_s \nabla \cdot [\mathbf{F}_m(\mathbf{r}) g(\mathbf{r}_s | \mathbf{r}')] ds = \oint_c \hat{n}_l \cdot \mathbf{F}_m(\mathbf{r}) g(\mathbf{r}_s | \mathbf{r}') dl = 0. \quad (2.9)$$

Therefore, C reduces to,

$$C = - \int_{s'} \nabla' \cdot \mathbf{J}(\mathbf{r}') \int_s \nabla \cdot \mathbf{F}_m(\mathbf{r}) g(\mathbf{r}_s | \mathbf{r}') ds ds'.$$

Then, after switching order of integration, we have

$$C = \int_s \int_{s'} \nabla \cdot \mathbf{F}_m(\mathbf{r}) \nabla' \cdot \mathbf{J}(\mathbf{r}') g(\mathbf{r}_s | \mathbf{r}') ds' ds. \quad (2.10)$$



Introduce an incident electric field as

$$\begin{aligned}\mathbf{E}^i(\mathbf{r}) &= \hat{e} e^{-jk_o(\hat{k}^i \cdot \mathbf{r})} \text{ where} \\ \hat{k}^i &= -\hat{r} = -\hat{x} \sin \theta_i \cos \phi_i - \hat{y} \sin \theta_i \sin \phi_i - \hat{z} \cos \theta_i \\ \mathbf{r} &= \hat{x}x + \hat{y}y + \hat{z}z \\ \therefore \hat{k}^i \cdot \mathbf{r} &= -x \sin \theta_i \cos \phi_i - y \sin \theta_i \sin \phi_i - z \cos \theta_i \text{ and} \\ \hat{e} &= \hat{\theta}_i \cos \alpha + \hat{\phi}_i \sin \alpha.\end{aligned}$$

Incorporate asymptotic phase (AP) expansion and testing functions as discussed in section 2.2 using coefficient  $\beta_m$  describing the amount of phase. The testing function becomes,

$$\mathbf{F}_m(\mathbf{r}) = \mathbf{f}_m(\mathbf{r}) e^{-j\beta_m(\hat{k}^i \cdot \mathbf{r})}. \quad (2.11)$$

Expanding the current as the sum of the currents over all N edges,

$$\mathbf{J}(\mathbf{r}') = \sum_{n=1}^N J_n \mathbf{f}_n(\mathbf{r}') e^{-j\beta_n(\hat{k}^i \cdot \mathbf{r}')}. \quad (2.12)$$

Therefore A, B, and C (redefining C by pulling out a minus sign) can be written so that

$$A = j\omega\mu \sum_{n=1}^N J_n \left[ B - \frac{1}{k_o^2} C \right] \text{ where}$$

$$A = \int_s \mathbf{f}_m(\mathbf{r}) \cdot \hat{e} e^{-j(k_o + \beta_m)\hat{k}^i \cdot \mathbf{r}} ds \quad (2.13)$$

$$B = \int_s \int_{s'} \mathbf{f}_m(\mathbf{r}) \mathbf{f}_n(\mathbf{r}') g(\mathbf{r}_s | \mathbf{r}') e^{-j\hat{k}^i \cdot (\beta_m \mathbf{r} + \beta_n \mathbf{r}')} ds' ds \quad (2.14)$$

$$C = \int_s \int_{s'} C_{\text{integrand}} g(\mathbf{r}_s | \mathbf{r}') ds' ds \quad (2.15)$$

where

$$C_{\text{integrand}} = \nabla \cdot \left[ \mathbf{f}_m(\mathbf{r}) e^{-j\beta_m(\hat{k}^i \cdot \mathbf{r})} \right] \nabla' \cdot \left[ \mathbf{f}_n(\mathbf{r}') e^{-j\beta_n(\hat{k}^i \cdot \mathbf{r}')} \right]. \quad (2.16)$$

Using the product rule for differentiation,

$$\nabla \cdot \left[ \mathbf{f}_m(\mathbf{r}) e^{-j\beta_m(\hat{k}^i \cdot \mathbf{r})} \right] = \mathbf{f}_m(\mathbf{r}) \cdot \nabla \left[ e^{-j\beta_m(\hat{k}^i \cdot \mathbf{r})} \right] + e^{-j\beta_m(\hat{k}^i \cdot \mathbf{r})} \nabla \cdot \mathbf{f}_m(\mathbf{r}).$$

Then, differentiating,

$$\begin{aligned} \nabla e^{-j\beta_m(\hat{k}^i \cdot \mathbf{r})} &= \nabla e^{j\beta_m(x \sin \theta_i \cos \phi_i + y \sin \theta_i \sin \phi_i + z \cos \theta_i)} \\ &= j\beta_m(x \sin \theta_i \cos \phi_i + y \sin \theta_i \sin \phi_i + z \cos \theta_i) e^{-j\beta_m(\hat{k}^i \cdot \mathbf{r})} \\ &= -j\beta_m \hat{k}^i e^{-j\beta_m(\hat{k}^i \cdot \mathbf{r})} \end{aligned}$$

which means

$$\nabla \cdot \left[ \mathbf{f}_m(\mathbf{r}) e^{-j\beta_m(\hat{k}^i \cdot \mathbf{r})} \right] = \left( \nabla \cdot \mathbf{f}_m(\mathbf{r}) - \mathbf{f}_m(\mathbf{r}) \cdot j\beta_m \hat{k}^i \right) e^{-j\beta_m(\hat{k}^i \cdot \mathbf{r})}. \quad (2.17)$$

Thus, by substitution of (2.17) into (2.16),

$$C_{\text{integrand}} = \frac{\left( \nabla \cdot \mathbf{f}_m(\mathbf{r}) - \mathbf{f}_m(\mathbf{r}) \cdot j\beta_m \hat{k}^i \right) \left( \nabla' \cdot \mathbf{f}_n(\mathbf{r}') - \mathbf{f}_n(\mathbf{r}') \cdot j\beta_n \hat{k}^i \right)}{e^{j\hat{k}^i \cdot (\beta_m \mathbf{r} + \beta_n \mathbf{r}')}}. \quad (2.18)$$

For notational simplicity, define

$$\tilde{g}(\mathbf{r} | \mathbf{r}') = g(\mathbf{r} | \mathbf{r}') e^{-j\hat{k}^i \cdot (\beta_m \mathbf{r} + \beta_n \mathbf{r}')} \quad (2.19)$$

Multiplying the numerator of  $C_{\text{integrand}}$  yields

$$\begin{aligned}
& \left( \nabla \cdot \mathbf{f}_m(\mathbf{r}) - \mathbf{f}_m(\mathbf{r}) \cdot j\beta_m \hat{k}^i \right) \left( \nabla' \cdot \mathbf{f}_n(\mathbf{r}') - \mathbf{f}_n(\mathbf{r}') \cdot j\beta_n \hat{k}^i \right) \\
&= \nabla \cdot \mathbf{f}_m(\mathbf{r}) (\nabla' \cdot \mathbf{f}_n(\mathbf{r}')) - \left( \mathbf{f}_m(\mathbf{r}) \cdot j\beta_m \hat{k}^i \right) \nabla' \cdot \mathbf{f}_n(\mathbf{r}') \\
&\quad - \nabla \cdot \mathbf{f}_m(\mathbf{r}) \left( \mathbf{f}_n(\mathbf{r}') \cdot j\beta_n \hat{k}^i \right) + \left( \mathbf{f}_m(\mathbf{r}) \cdot j\beta_m \hat{k}^i \right) \left( \mathbf{f}_n(\mathbf{r}') \cdot j\beta_n \hat{k}^i \right) \\
&= \nabla \cdot \mathbf{f}_m(\mathbf{r}) [\nabla' \cdot \mathbf{f}_n(\mathbf{r}')] - j\beta_m \hat{k}^i \cdot \mathbf{f}_m(\mathbf{r}) [\nabla' \cdot \mathbf{f}_n(\mathbf{r}')] \\
&\quad - j\beta_n \hat{k}^i \cdot \mathbf{f}_n(\mathbf{r}') [\nabla \cdot \mathbf{f}_m(\mathbf{r})] - \beta_m \beta_n \left[ \hat{k}^i \cdot \mathbf{f}_m(\mathbf{r}) \right] \left[ \hat{k}^i \cdot \mathbf{f}_n(\mathbf{r}') \right].
\end{aligned}$$

Thus,

$$C = \int_s \int_{s'} \tilde{g}(\mathbf{r} | \mathbf{r}') \left\{ \begin{array}{l} \nabla \cdot \mathbf{f}_m(\mathbf{r}) [\nabla' \cdot \mathbf{f}_n(\mathbf{r}')] \\ -j\beta_m \hat{k}^i \cdot \mathbf{f}_m(\mathbf{r}) [\nabla' \cdot \mathbf{f}_n(\mathbf{r}')] \\ -j\beta_n \hat{k}^i \cdot \mathbf{f}_n(\mathbf{r}') [\nabla \cdot \mathbf{f}_m(\mathbf{r})] \\ -\beta_m \beta_n \left[ \hat{k}^i \cdot \mathbf{f}_m(\mathbf{r}) \right] \left[ \hat{k}^i \cdot \mathbf{f}_n(\mathbf{r}') \right] \end{array} \right\} ds' ds. \quad (2.20)$$

Combining A, B, C back into  $A = j\omega\mu \sum_{n=1}^N J_n \left[ B - \frac{1}{k_o^2} C \right]$  results in

$$\int_s \mathbf{f}_m(\mathbf{r}) \cdot \hat{e} e^{-j(k_o + \beta_m) \hat{k}^i \cdot \mathbf{r}} ds = j\omega\mu \sum_{n=1}^N J_n Z_{nm}^{EFIE}, \quad (2.21)$$

where

$$Z_{nm}^{EFIE} = \int_s \int_{s'} \tilde{g}(\mathbf{r} | \mathbf{r}') \left[ \mathbf{f}_m(\mathbf{r}) \mathbf{f}_n(\mathbf{r}') + \frac{1}{k_o} \begin{pmatrix} -\nabla \cdot \mathbf{f}_m(\mathbf{r}) [\nabla' \cdot \mathbf{f}_n(\mathbf{r}')] \\ + j\beta_m \hat{k}^i \cdot \mathbf{f}_m(\mathbf{r}) [\nabla' \cdot \mathbf{f}_n(\mathbf{r}')] \\ + j\beta_n \hat{k}^i \cdot \mathbf{f}_n(\mathbf{r}') [\nabla \cdot \mathbf{f}_m(\mathbf{r})] \\ + \beta_m \beta_n [\hat{k}^i \cdot \mathbf{f}_m(\mathbf{r})] [\hat{k}^i \cdot \mathbf{f}_n(\mathbf{r}')] \end{pmatrix} \right] ds' ds \quad (2.22)$$

is the EFIE impedance matrix. For future reference, rewrite (2.21) and (2.22) in a form convenient for discussion;

$$\int_s \mathbf{f}_m(\mathbf{r}) \cdot \hat{e} e^{-j(k_o + \beta_m) \hat{k}^i \cdot \mathbf{r}} ds = j\omega\mu \sum_{n=1}^N J_n \int_s \int_{s'} \tilde{g}(\mathbf{r} | \mathbf{r}') \tilde{Z}_{nm}^{EFIE} ds' ds \quad (2.23)$$

where

$$\tilde{Z}_{nm}^{EFIE} = \mathbf{f}_m(\mathbf{r}) \mathbf{f}_n(\mathbf{r}') + \frac{1}{k_o^2} \begin{pmatrix} -\nabla \cdot \mathbf{f}_m(\mathbf{r}) [\nabla' \cdot \mathbf{f}_n(\mathbf{r}')] \\ + j\beta_m \hat{k}^i \cdot \mathbf{f}_m(\mathbf{r}) [\nabla' \cdot \mathbf{f}_n(\mathbf{r}')] \\ + j\beta_n \hat{k}^i \cdot \mathbf{f}_n(\mathbf{r}') [\nabla \cdot \mathbf{f}_m(\mathbf{r})] \\ + \beta_m \beta_n [\hat{k}^i \cdot \mathbf{f}_m(\mathbf{r})] [\hat{k}^i \cdot \mathbf{f}_n(\mathbf{r}')] \end{pmatrix} \quad (2.24)$$

and from (2.19),

$$\tilde{g}(\mathbf{r} | \mathbf{r}') = g(\mathbf{r} | \mathbf{r}') e^{-j\hat{k}^i \cdot (\beta_m \mathbf{r} + \beta_n \mathbf{r}')}.$$

Note that if the testing and expansion functions are RWG, then  $\beta_m$  and  $\beta_n$  are zero. In

this case (2.23) and (2.24) reduce to the familiar [1, 2, 3, 8] expression,

$$\begin{aligned}
& \int_s \mathbf{f}_m(\mathbf{r}) \cdot \hat{\mathbf{e}} e^{-jk_o \hat{\mathbf{k}}^i \cdot \mathbf{r}} ds \\
&= j\omega\mu \sum_{n=1}^N J_n \int_s \int_{s'} g(\mathbf{r} | \mathbf{r}') \left[ \frac{\mathbf{f}_m(\mathbf{r}) \mathbf{f}_n(\mathbf{r}')}{-\frac{\nabla \cdot \mathbf{f}_m(\mathbf{r}) [\nabla' \cdot \mathbf{f}_n(\mathbf{r}')] }{k_o}} \right] ds' ds. \quad (2.25)
\end{aligned}$$

If either the testing or the expansion function is AP, one of the middle two terms in the brackets of (2.24) are added. For matrix elements where both testing and expansion functions are AP, we must compute all the terms in (2.24); the last three of which must be computed at each incident angle. It is important to note that in all cases, the impedance matrix is symmetric, thus we can use specialized solution methods.

#### 4. Magnetic Field Integral Equation Method of Moments

A similar application of the method of moments can be applied to the magnetic field integral. Recall the MFIE from equation (1.25),

$$\hat{\mathbf{n}} \times \mathbf{H}^i(\mathbf{r}) = \frac{\mathbf{J}_s(\mathbf{r})}{2} - \oint_{s^+} \hat{\mathbf{n}} \times \mathbf{J}_s(\mathbf{r}') \times \nabla' g(\mathbf{r} | \mathbf{r}') ds'. \quad (2.26)$$

The  $s^+$  in equation (2.26) is a reminder that the MFIE is to be evaluated  $\epsilon > 0$  distance outside the surface, hence should be evaluated in the principal value sense. We test the MFIE, as with the EFIE, with

$$\mathbf{F}_m(\mathbf{r}) = \mathbf{f}_m(\mathbf{r}) e^{-j\beta_m(\hat{\mathbf{k}}^i \cdot \mathbf{r})}$$

and expanding the current as the sum of the currents over all  $N$  edges,

$$\mathbf{J}(\mathbf{r}') = \sum_{n=1}^N J_n \mathbf{f}_n(\mathbf{r}') e^{-j\beta_n(\hat{\mathbf{k}}^i \cdot \mathbf{r}')},$$

yielding,

$$\begin{aligned}
& \int_s \mathbf{f}_m(\mathbf{r}) \cdot \hat{\mathbf{n}} \times \mathbf{H}^i(\mathbf{r}') e^{-j\beta_m(\hat{\mathbf{k}}^i \cdot \mathbf{r})} ds \\
&= \frac{1}{2} \int_s \mathbf{f}_m(\mathbf{r}) \cdot \sum_{n=1}^N J_n \mathbf{f}_n(\mathbf{r}') e^{-j\hat{\mathbf{k}}^i \cdot (\beta_m \mathbf{r} + \beta_n \mathbf{r}')} ds \\
&\quad - \int_s \mathbf{f}_m(\mathbf{r}) \cdot \hat{\mathbf{n}} \times \oint_{s^+} \sum_{n=1}^N J_n \mathbf{f}_n(\mathbf{r}') \times [\nabla' g(\mathbf{r} | \mathbf{r}')] e^{-j\hat{\mathbf{k}}^i \cdot (\beta_m \mathbf{r} + \beta_n \mathbf{r}')} ds' ds \\
&\Rightarrow F_m^{MFIE} = \sum_{n=1}^N J_n Z_{nm}^{MFIE} \ni \\
&\quad Z_{nm}^{MFIE} = \int_s \left[ \begin{aligned} & \frac{1}{2} \mathbf{f}_m(\mathbf{r}) \cdot \mathbf{f}_n(\mathbf{r}') e^{-j\hat{\mathbf{k}}^i \cdot (\beta_m \mathbf{r} + \beta_n \mathbf{r}')} \\ & - \mathbf{f}_m(\mathbf{r}) \cdot \hat{\mathbf{n}} \times \oint_{s^+} \mathbf{f}_n(\mathbf{r}') \times \nabla' \tilde{g}(\mathbf{r} | \mathbf{r}') ds' \end{aligned} \right] ds.
\end{aligned}$$

Again, we are using the notation from (2.19). Our first observation is the asymmetry of the MFIE impedance matrix. The  $Z^{MFIE}$  is more difficult than the EFIE to evaluate due to this asymmetry and performing the principal value sense integration.

## CHAPTER 3: BASIS FUNCTION SPECIFICATION

To implement the preceding impedance matrix in a numerical solver, we still need to specify the spatial distribution of the basis functions,  $\mathbf{f}$ . Additionally, we need to evaluate the singular integrals when the source and observation elements coalesce. This chapter uses the Rao-Wilton-Glisson [1] definition for sub-domain vector basis functions to write the impedance matrix, in particular the electric field integral equation impedance matrix, in a form appropriate for numerical implementation. We then discuss the self-cell problem and its resolution for the case of flat triangles.

### *1. Sub-domain Vector Basis Functions*

As described in Chapter 2,  $\mathbf{f}_n$  and  $\mathbf{f}_m$  are standard RWG basis functions. Recall that for asymptotic basis functions, we multiply the RWG function by the incident phase term. The final impedance matrix from Chapter 2 incorporates the combination of basis functions using the parameters  $\beta_m$  and  $\beta_n$ . One can see by inspection that if both the source and observation edge are RWG ( $\beta_n = \beta_m = 0$ ), the impedance matrix reduces to the familiar RWG MoM symmetric impedance matrix. As intended then, the phase factor is separated from the RWG basis function in the impedance matrix equation. For numerical implementation, at this point we need only substitute the RWG basis function definition for  $\mathbf{f}_m(\mathbf{r})$  and  $\mathbf{f}_n(\mathbf{r}')$ .

As defined in [1], RWG sub-domain basis functions for triangle patches effectively model the current on a scatterer. These basis functions describe the expanded current only over two triangles sharing a common edge indicated by the expansion and testing indices ( $n$  or  $m$ ) and are zero elsewhere, hence the term sub-domain.

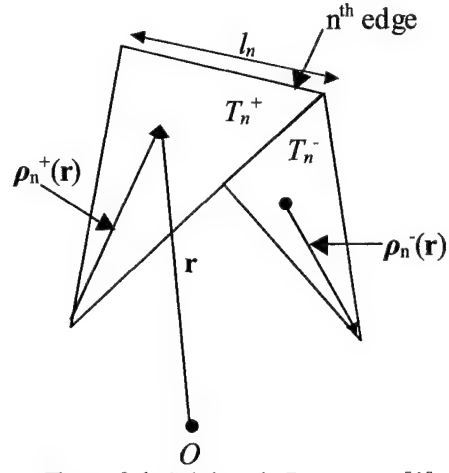


Figure 3.1: Subdomain Parameters [1]

Figure 3.1 illustrates the nature of these basis functions and the associated parameters for the  $n^{\text{th}}$  interior edge shared by triangles  $T_n^+$  and  $T_n^-$ . A point in either triangle is described by either  $\mathbf{r}$  from the global origin or  $\boldsymbol{\rho}_n^\pm(\mathbf{r})$ , a local position vector from emanating from the free vertex (e.g. the vertex opposite the  $n^{\text{th}}$  edge) of the triangle on which the point is located. Notice the direction of  $\boldsymbol{\rho}_n^\pm(\mathbf{r})$  from the free vertex of  $T_n^+$  across the shared edge towards the free vertex of  $T_n^-$ . This establishes positive current reference direction from the  $T_n^+$  to  $T_n^-$ . As seen in figure 3.1,  $l_n$  is the length of the  $n^{\text{th}}$  edge and  $A_n^\pm$  is the area of triangle  $T_n^\pm$ . The basis function  $\mathbf{f}_n(\mathbf{r})$  for the  $n^{\text{th}}$  edge is then defined as

$$\mathbf{f}_n(\mathbf{r}) = \begin{cases} \frac{l_n \boldsymbol{\rho}_n^+(\mathbf{r})}{2A_n^+}, & \text{for } \mathbf{r} \text{ in } T_n^+ \\ \frac{-l_n \boldsymbol{\rho}_n^-(\mathbf{r})}{2A_n^-}, & \text{for } \mathbf{r} \text{ in } T_n^- \\ 0, & \text{elsewhere,} \end{cases} \quad (3.1)$$



where the surface divergence of  $\mathbf{f}_n(\mathbf{r})$ , proportional to the surface charge density associated with the basis element, is given by

$$\nabla \cdot \mathbf{f}_n(\mathbf{r}) = \begin{cases} \frac{l_n}{A_n^+}, & \text{for } \mathbf{r} \text{ in } T_n^+ \\ \frac{-l_n}{A_n^-}, & \text{for } \mathbf{r} \text{ in } T_n^- \\ 0, & \text{elsewhere.} \end{cases} \quad (3.2)$$

Some properties that make the basis function  $\mathbf{f}_n(\mathbf{r})$  particularly suited to approximating the surface current are detailed in [1] and stated here.

1. The current has no component normal to the boundary of the surface formed by the triangle pair  $T_n^+$ ,  $T_n^-$ . Thus, no line charges exist along this boundary.
2. The current component normal to the  $n^{\text{th}}$  edge is constant and continuous across the edge. It is therefore implied that all edges of the triangle pair are free of line charges.
3. Due to (3.2), the charge density is constant in each triangle and the total charge associated with the pair is zero.

## 2. Impedance Matrix

We then substitute the definition for RWG basis function into the impedance matrix form of the EFIE established previously (2.24). Recall

$$\int_s \mathbf{f}_m(\mathbf{r}) \cdot \hat{\mathbf{e}} e^{-j(k_o + \beta_m) \hat{\mathbf{k}}^i \cdot \mathbf{r}} ds = j\omega\mu \sum_{n=1}^N J_n \int_s \int_{s'} \tilde{g}(\mathbf{r} | \mathbf{r}') \tilde{Z}_{nm}^{EFIE} ds' ds$$

where

$$\tilde{Z}_{nm}^{EFIE} = \mathbf{f}_m(\mathbf{r})\mathbf{f}_n(\mathbf{r}') + \frac{1}{k_o^2} \begin{pmatrix} -\nabla \cdot \mathbf{f}_m(\mathbf{r}) [\nabla \cdot \mathbf{f}_n(\mathbf{r}')] \\ + j\beta_m \hat{k}^i \cdot \mathbf{f}_m(\mathbf{r}) [\nabla \cdot \mathbf{f}_n(\mathbf{r}')] \\ + j\beta_n \hat{k}^i \cdot \mathbf{f}_n(\mathbf{r}') [\nabla \cdot \mathbf{f}_m(\mathbf{r})] \\ + \beta_m \beta_n [\hat{k}^i \cdot \mathbf{f}_m(\mathbf{r})] [\hat{k}^i \cdot \mathbf{f}_n(\mathbf{r}')] \end{pmatrix}$$

and

$$\tilde{g}(\mathbf{r} | \mathbf{r}') = \frac{1}{4\pi R} e^{-jk_o R} e^{-j\hat{k}^i \cdot (\beta_m \mathbf{r} + \beta_n \mathbf{r}')} , R = |\mathbf{r} - \mathbf{r}'|.$$

Observe the form of the above equation is  $[Z]\{J\} = \{V\}$ , where  $[Z]$  is an  $N \times N$  system and  $N$  is the number of edges in the mesh. The tested left hand side of the EFIE becomes

$$\int_s \mathbf{f}_m(\mathbf{r}) \cdot \hat{e} e^{-j(k_o + \beta_m)\hat{k}^i \cdot \mathbf{r}} ds = \frac{l_m l_m}{2A_m^\pm} \int_{T_m^+ + T_m^-} \boldsymbol{\rho}^\pm(\mathbf{r}) \cdot \hat{e} e^{-j(k_o + \beta_m)\hat{k}^i \cdot \mathbf{r}} ds. \quad (3.3)$$

Here we have introduced the sign carrying parameter

$$l_i = \begin{cases} 1, & \text{for } \mathbf{r} \text{ in } T_i^+ \\ -1, & \text{for } \mathbf{r} \text{ in } T_i^- \end{cases} \quad (3.4)$$

and used  $\pm$  with the top sign for  $\mathbf{r}$  in  $T_n^+$  and the bottom sign for  $\mathbf{r}$  in  $T_n^-$ . The right hand side consists of a constant ( $j\omega\mu$ ) multiplying the unknown current expansion coefficient column vector ( $J_n$ ) times a matrix  $Z_{nm}^{EFIE}$ . Matrix elements associated with the  $n^{\text{th}}$  row and  $m^{\text{th}}$  column are then given by

$$Z_{nm}^{EFIE} = \int_{T_m^+ + T_m^-} \int_{T_n^+ + T_n^-} \frac{1}{4\pi R} e^{-jk_o R} e^{-j\hat{k}^i \cdot (\beta_m \mathbf{r} + \beta_n \mathbf{r}')} \tilde{Z}_{nm}^{EFIE} ds' ds \quad (3.5)$$

with

$$\begin{aligned}
\tilde{Z}_{nm}^{EFIE} &= \int \mathbf{f}_m(\mathbf{r})\mathbf{f}_n(\mathbf{r}') + \frac{1}{k_o^2} \begin{pmatrix} -\nabla \cdot \mathbf{f}_m(\mathbf{r})[\nabla \cdot \mathbf{f}_n(\mathbf{r}')] \\ +j\beta_m \hat{k}^i \cdot \mathbf{f}_m(\mathbf{r})[\nabla \cdot \mathbf{f}_n(\mathbf{r}')] \\ +j\beta_n \hat{k}^i \cdot \mathbf{f}_n(\mathbf{r}')[\nabla \cdot \mathbf{f}_m(\mathbf{r})] \\ +\beta_m \beta_n [\hat{k}^i \cdot \mathbf{f}_m(\mathbf{r})][\hat{k}^i \cdot \mathbf{f}_n(\mathbf{r}')] \end{pmatrix} \\
&= \frac{\iota_m l_m \boldsymbol{\rho}_m^\pm(\mathbf{r})}{2A_m^\pm} \cdot \frac{\iota_n l_n \boldsymbol{\rho}_n^\pm(\mathbf{r}')}{2A_n^\pm} + \frac{1}{k_o^2} \begin{pmatrix} -\frac{\iota_m l_m \iota_n l_n}{A_m^\pm A_n^\pm} \\ +j\beta_m \hat{k}^i \cdot \frac{\iota_m l_m \boldsymbol{\rho}_m^\pm(\mathbf{r})}{2A_m^\pm} \frac{\iota_n l_n}{A_n^\pm} \\ +j\beta_n \hat{k}^i \cdot \frac{\iota_n l_n \boldsymbol{\rho}_n^\pm(\mathbf{r}')}{2A_n^\pm} \frac{\iota_m l_m}{A_m^\pm} \\ +\beta_m \beta_n \left[ \hat{k}^i \cdot \frac{\iota_m l_m \boldsymbol{\rho}_m^\pm(\mathbf{r})}{2A_m^\pm} \right] \left[ \hat{k}^i \cdot \frac{\iota_n l_n \boldsymbol{\rho}_n^\pm(\mathbf{r}')}{2A_n^\pm} \right] \end{pmatrix} \\
&= \frac{\iota_m l_m \iota_n l_n}{4A_m^\pm A_n^\pm} \boldsymbol{\rho}_m^\pm(\mathbf{r}) \cdot \boldsymbol{\rho}_n^\pm(\mathbf{r}') + \frac{\iota_m l_m \iota_n l_n}{k_o^2 A_m^\pm A_n^\pm} \begin{pmatrix} -1 + \frac{j}{2} \beta_m \hat{k}^i \cdot \boldsymbol{\rho}_m^\pm(\mathbf{r}) + \frac{j}{2} \beta_n \hat{k}^i \cdot \boldsymbol{\rho}_n^\pm(\mathbf{r}') \\ +\beta_m \beta_n \frac{1}{4} [\hat{k}^i \cdot \boldsymbol{\rho}_m^\pm(\mathbf{r})][\hat{k}^i \cdot \boldsymbol{\rho}_n^\pm(\mathbf{r}')] \end{pmatrix} \\
&= \frac{\iota_m l_m \iota_n l_n}{4k_o^2 A_m^\pm A_n^\pm} \begin{pmatrix} k_o^2 \boldsymbol{\rho}_m^\pm(\mathbf{r}) \cdot \boldsymbol{\rho}_n^\pm(\mathbf{r}') - 4 + j2\beta_m \hat{k}^i \cdot \boldsymbol{\rho}_m^\pm(\mathbf{r}) \\ +j2\beta_n \hat{k}^i \cdot \boldsymbol{\rho}_n^\pm(\mathbf{r}') + \beta_m \beta_n [\hat{k}^i \cdot \boldsymbol{\rho}_m^\pm(\mathbf{r})][\hat{k}^i \cdot \boldsymbol{\rho}_n^\pm(\mathbf{r}')] \end{pmatrix}.
\end{aligned}$$

In evaluation of  $\tilde{Z}_{nm}^{EFIE}$ , it is useful to

recognize that  $\boldsymbol{\rho}_i^\pm(\mathbf{r}), i \in \{m, n\}$  are expressed

in global coordinates as  $\boldsymbol{\rho}_i^\pm(\mathbf{r}) = \pm(\mathbf{r} - \mathbf{r}_i)$

where  $\mathbf{r}_i$  is the global position vector to the vertex opposite edge  $i$  on  $T_i^\pm$  as shown in

Figure 3.2.

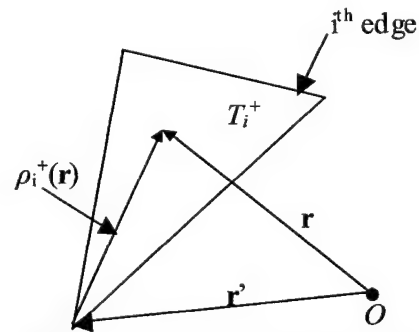


Figure 3.2: Local Position in Terms of Global Position Vectors

### 3. Singularities

Equation (3.5) may be readily evaluated numerically unless the source and observation

edges are close. We resolve the singularity as in [7], with  $e^{-jk^i \cdot (\beta_m \mathbf{r} + \beta_n \mathbf{r}')}$  suppressed in the integrand of each term,

$$\begin{aligned} \int_{T_i^\pm} \rho_i^\pm(\mathbf{r}') \frac{e^{-jk_o R}}{R} ds' &= \int_{T_i^\pm} \rho_i^\pm(\mathbf{r}') \frac{e^{-jk_o R} - 1}{R} ds' \\ &+ \int_{T_i^\pm} \frac{(\boldsymbol{\rho}' - \boldsymbol{\rho})}{R} ds' + (\boldsymbol{\rho} - \boldsymbol{\rho}_i) \int_{T_i^\pm} \frac{1}{R} ds' \end{aligned} \quad (3.6)$$

where  $\boldsymbol{\rho}, \boldsymbol{\rho}', \boldsymbol{\rho}_i$  are projections of position vectors  $\mathbf{r}, \mathbf{r}', \mathbf{r}_i$  respectively onto triangle  $T_i^\pm$ .

The first integral is bounded, so it can be numerically integrated, while the second two can be evaluated analytically. Similarly, the scalar integrals can be written

$$\int_{T_i^\pm} \frac{e^{-jk_o R}}{R} ds' = \int_{T_i^\pm} \frac{e^{-jk_o R} - 1}{R} ds' + \int_{T_i^\pm} \frac{1}{R} ds'. \quad (3.7)$$

### 4. Coding

The code used for testing was primarily a modified version of the program, *TriMom*, by Dr. Pamela Haddad [8]\* implemented at Michigan State University. The modified code, called *HotPoppa*, is a FORTAN based numerical solver. It allows for solution of the EFIE using the basis function development included in the previous chapter. It was additionally modified to import .grd mesh files created by SkyMesh2™ as well as SDRC IDEAS Universal files (.unv).

\*Dr. Pamela Haddad performed this work while on NSF Graduate Fellowship at the University of Michigan. She is now a mentor of the technical staff at MIT's Lincoln Laboratory.

## CHAPTER 4: RESULTS

This chapter presents details regarding numerical solutions of the theory presented above. Results for two different size square plates, a kite, and the EMCC mini-arrow are discussed and compared. We shall analyze the kite in extensive detail as we explore several implications of the mixed basis function method. Additionally, convergence comparisons between various basis function implementations along with mesh density analysis are presented for the kite. Radar cross section (RCS) values are used for comparison as they indicate the scattering characteristics of the object.

### 1. Square Plate

Two square plates are initially considered showing the potential for mixed basis function implementation to perform accurately as proposed. For a  $4 \times 4$  wavelength plate, a tenth of a wavelength edge length mesh leads to 2240 unknowns while the graded ( or non-uniform) mesh reduces the number of unknowns to 1870. Figure 4.1 shows monostatic RCS results and the graded

mesh for the  $4 \times 4$  wavelength plate. We observe excellent agreement. The reference line shows results for tenth of a wavelength sampling over the entire square using

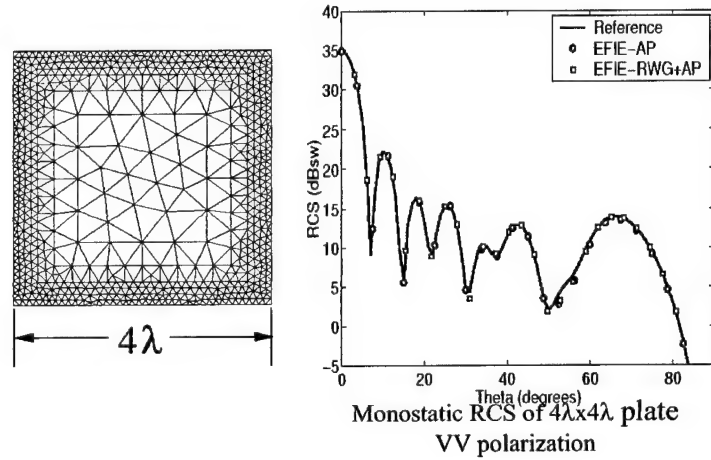
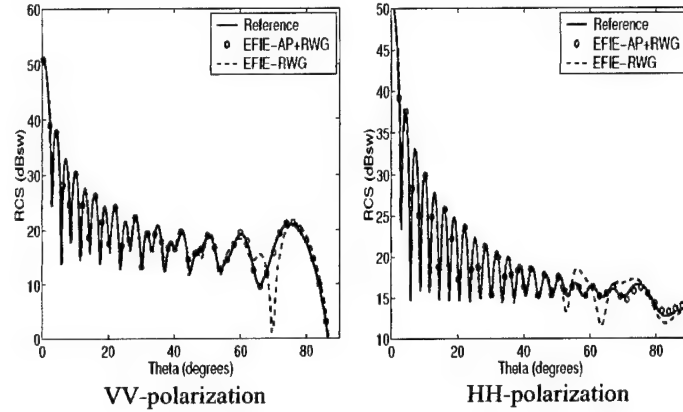


Figure 4.1: Sample results for a  $4\lambda \times 4\lambda$  plate.[3]

only RWG basis and testing functions. EFIE-AP refers to AP basis and testing functions on the pictured graded mesh while EFIE-RWG + AP shows the results for using RWG functions in the outer region of the graded mesh and



**Figure 4.2:** Scattering by a  $10\lambda \times 10\lambda$  plate.[3]

AP functions in the inner region. For a  $10 \times 10$  wavelength plate, tenth of a wavelength sampling results in a mesh of 14,600 edges while a graded mesh has only 4,792 edges (67% reduction). Again, the results are very promising as we see in Figure 4.2.

## 2. The Kite: Description

The kite is an infinitesimally thin PEC surface in free space. (Figure 4.3) Its length of 23.495 cm is approximately eight wavelengths at ten GHz.

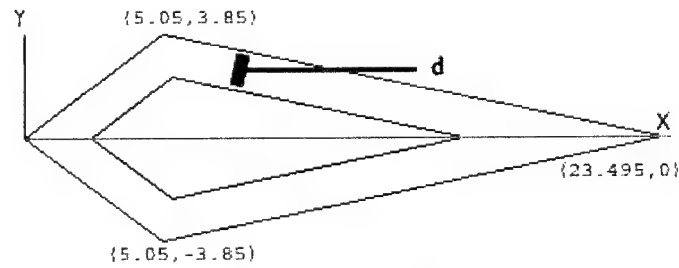


**Figure 4.3:** The Kite

The kite is one face of the EMCC mini-arrow, an object studied in Section 4.4.

Additionally, we wish to define two ways of observing the kite for scattering solution discussion. Described using standard spherical coordinate basis, the following “cuts” describe the arc of incident and observation angles.

1. Waterline cut (WL): Figure 4.4

$$\theta = 90^\circ, \phi = 0^\circ \rightarrow 180^\circ$$

2. Over-the-Top cut (OTT): Figure 4.5

$$\theta = -90^\circ \rightarrow 90^\circ, \phi = 0^\circ$$

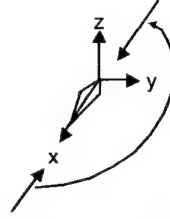


Figure 4.4: WL

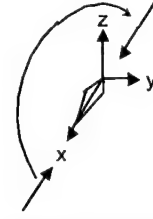


Figure 4.5: OTT

Note that these two perspectives use full advantage of the symmetry of the kite. For each perspective, we will consider theta and phi polarized incident waves. However, results are not presented for the WL cut theta polarization since an incident wave thus oriented induces no current. The three remaining cut/polarization combinations, over the top theta pol, over the top cut phi pol and waterline cut phi pol, will be abbreviated OTT-T, OTT-P, and WL-P respectively.

The kite presents an interesting geometry for method testing for several reasons.

1. It has features (relatively large, flat, and PEC) that take advantage of the methodology.
2. It is small enough to achieve numerical results in a reasonable amount of time at frequencies in the five to twelve GHz range.
3. It is the largest facet of the EMCC mini-arrow for which the community maintains experimental data. We extend our study to the three-dimensional mini-arrow in Section 4.4.

As with the square above, we break the kite into two regions, a proportional inner kite and a border region. Refer again to Figure 4.3. The inner region is formed by taking the

intersection of lines parallel to the kite edges and separated by a constant distance  $d$  from the edges. Due to geometry, and easily observed, the vertex points of the inner and outer kites are greater than  $d$  apart. One can specify  $d$  to determine the inner kite (after describing the outer kite). Appendix E contains calculations used to derive the vertices of the inner kite from the parameter  $d$ .

In general, we want to make  $d$  as small as possible because as we will see, a small  $d$  results in a smaller number of unknowns. However, to ensure accuracy, it is necessary to keep  $d$  near half a wavelength to account for edge conditions not incorporated in the AP basis functions. This is discussed further when we observe results.

Using Skymesh2™ to create a triangular mesh, we can define the edge elements for use in our numerical solution. The division of the kite into inner and outer regions provides two essential levels of control. We can independently control the mesh density in the two regions. This allows us to maintain approximately ten elements per wavelength in the border region and much less in the inner region. Skymesh2™ accomplishes a gradient transition in the inner region. Being able to control the mesh density in the two regions enables us to take full advantage of the different basis functions. The different regions in the mesh allow us to specify which type of basis function

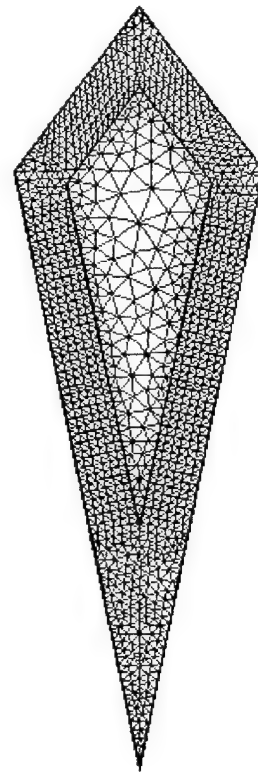


**Figure 4.6:** 10 GHz Kite Mesh



(specifically, the value of  $\beta$ ) used for elements in each region. Therefore, as mentioned in chapter 2, we can use a fine (ten element per wavelength) mesh with RWG basis functions near discontinuities (edges in the case of the kite) and AP basis functions in sparsely meshed regions away from the discontinuities. Note that this method differs from [3] where the basis function for an edge is determined by its length.

As we discuss kite results, we will use a mesh density factor for a given region or for the kite as a whole. This number is related to the mesh creation and is proportional to the number of elements per wavelength, but does not describe it directly. A factor of 12 roughly equates to a maximum element size of a tenth of a wavelength. Often the mesh density factor is presented as a pair specifying the entire kite and is written outer/inner. (e.g. A mesh density factor of 12/3 describes a fine outer mesh and a relatively sparse inner mesh.)

### ***3. The Kite: Results***

Several mesh configurations were solved using a variety of basis function combinations and slightly varying d-spacing for all three orientations (OTT-P, OTT-T, WL-P). A frequency of 5 GHz is used for code validation; 10 GHz is presented for RCS curve comparison while 12 GHz is used for a mesh density analysis. These selections are based on the element size relative to the kite, relative to a wavelength, and the total number of elements as it affects the run time.

Table 4.1 illustrates the size of the problem for various configurations.

The problem quickly becomes quite large with increasing frequency.

However, 12 GHz allowed for a larger difference and variation control of the inner mesh density lending itself to the mesh density analysis.

	Dist	Freq	Density	Nodes	Triangles	Edges
a		5	12/12	1447	674	1060
b	1.5	5	3/12	1267	584	925
c		10	12/12	5667	2734	4200
d	1.5	10	3/12	4523	2162	3342
e	1	10	3/12	3787	1794	2790
f	1.25	12	16/16	14294	6989	10641
g	1.25	12	14/14	10957	5340	8148
h	1.25	12	12/12	8091	3926	6008
i	1.25	12	12/9	6787	3274	5030
j	1.25	12	12/6	6027	2894	4460
k	1.25	12	12/2.8	5807	2784	4295

**Table 4.1:** Problem Size

#### **Code Validation Case:**

Initially, 5 GHz results were studied, however, the edge number reduction was minimal (1060 vs. 925). It was useful to see that using RWG in both regions, using AP in both regions, and using a combination (RWG outer, AP inner) all produced similar RCS values. The following results correspond to row (b) in table 4.1. The separation,  $d$ , is set to 1.5 cm because it becomes impractical to make it any larger from a meshing standpoint (the mesh becomes geometrically constricted). Setting  $d$  less than half a wavelength is not detrimental to the solution in this case.

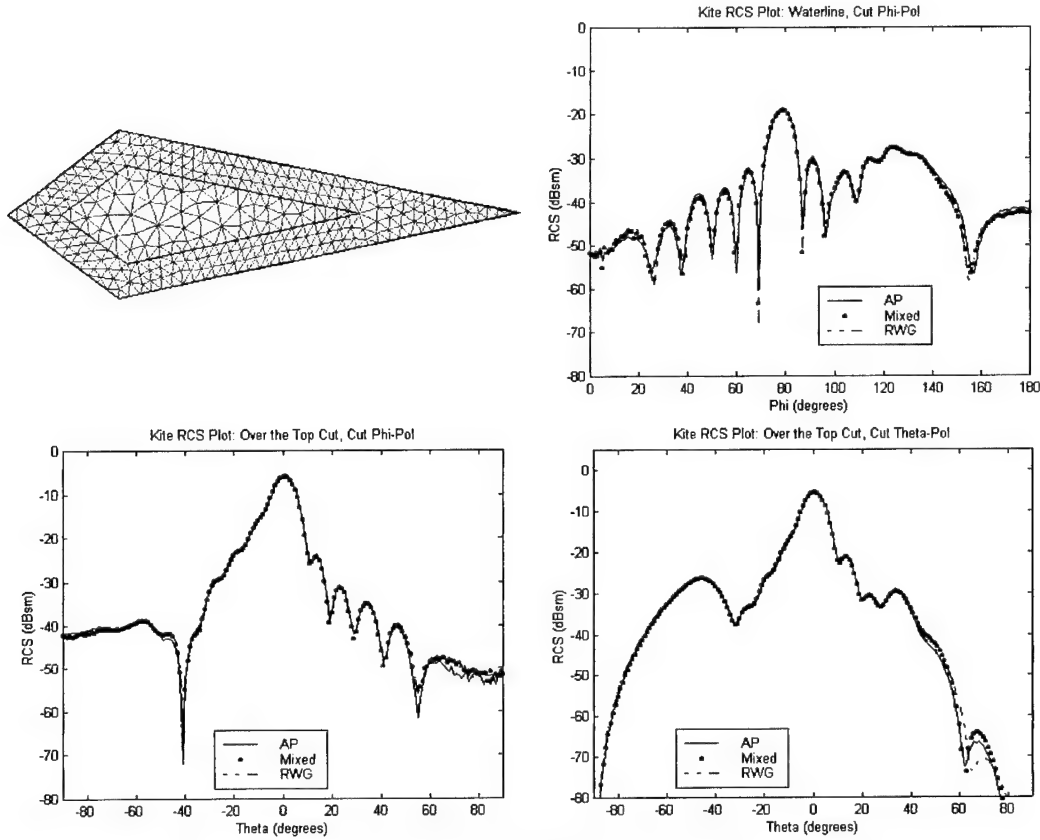
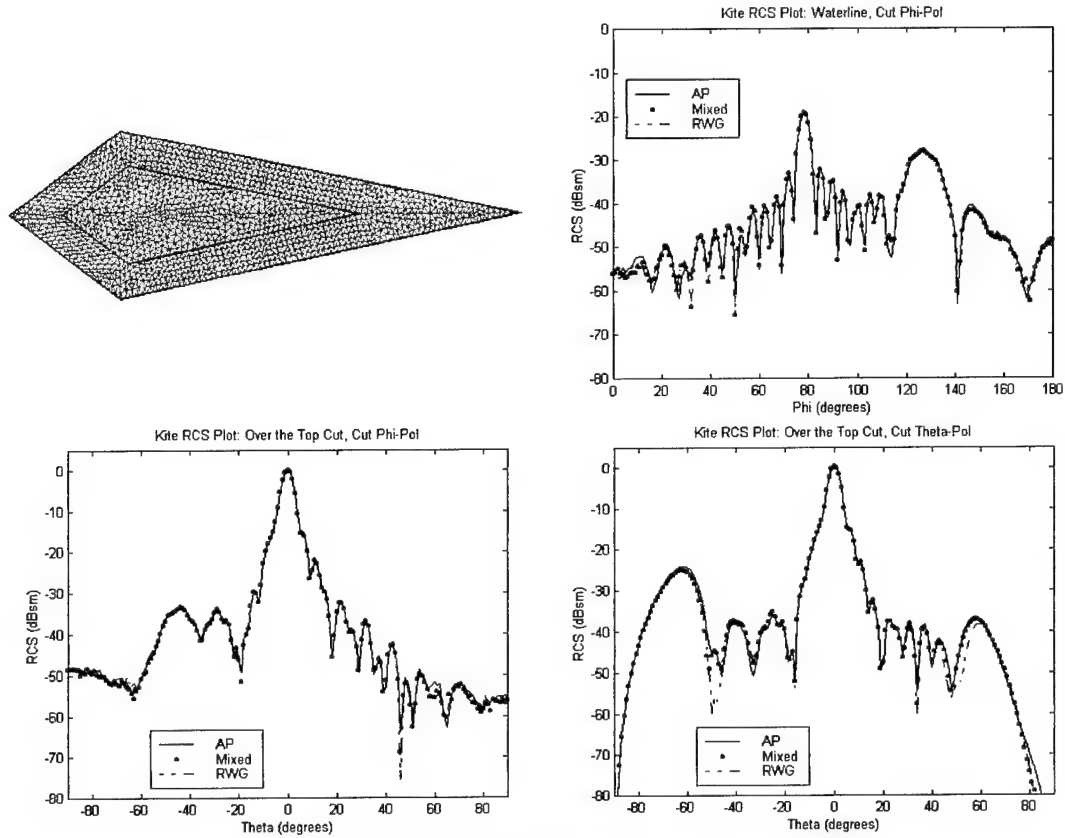


Figure 4.7: 5 GHz Kite RCS Plot,  $d = 1.5$  cm, Density Factor = 12/3

### RCS Curve Comparison:

For a frequency of 10 GHz, three different meshes were considered. The first (c in table 4.1) has a mesh density factor of 12/12, approximately ten edges per wavelength across both regions of the kite. RCS curves are shown in Figure 4.8. One can see that the three curves in each figure (AP only, RWG only, and mixed with AP inner and RWG outer) closely match each other. Some discrepancy (3dB max) is apparent in the OTT curves (Figures 4.11 and 4.12) in the  $-60$  to  $-40$  and  $40$  to  $60$  degree theta range. However, we can see that the mixed basis function method consistently matches AP only results for this implementation.



**Figure 4.8:** 10 GHz Kite RCS Plot, Mesh Density Factor = 12/12

The second 10 GHz experiment has a mesh density factor of 12/3 where the inner kite is sampled less. The separation  $d$  is 1.5 cm, or half a wavelength. In this case – (d) in table 4.1 – we observe a 20% reduction in unknowns. Figure 4.9 illustrates the element size verses position in the mesh. Figure 10 shows the RCS values for the various perspectives. In the waterline cut, we begin to see discrepancies in the 145-160 degree phi range where the RWG-only curve does not match the AP and mixed curves. The same mismatch is visible in the OTT cuts across a large range of theta angles with almost 10dB difference for certain angles. These mismatches are expected since RWG typically requires a minimum sampling of ten elements per wavelength over the entire surface for accurate results. Similar discrepancies exist for case (e) in table 4.1 where the border

region is shrunk to one cm (see figure 4.11). Notice that in case (e), the number of unknowns is reduced 33.5% as compared to (c).

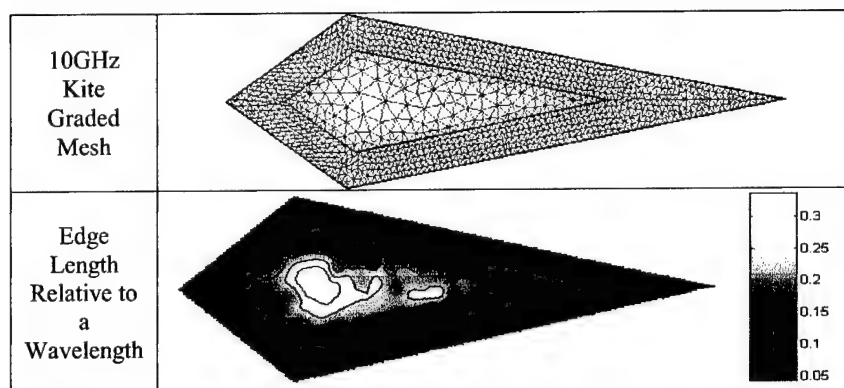


Figure 4.9: 10 GHz Kite,  $d = 1.5\text{cm}$ , Mesh Density Factor =  $12/3$

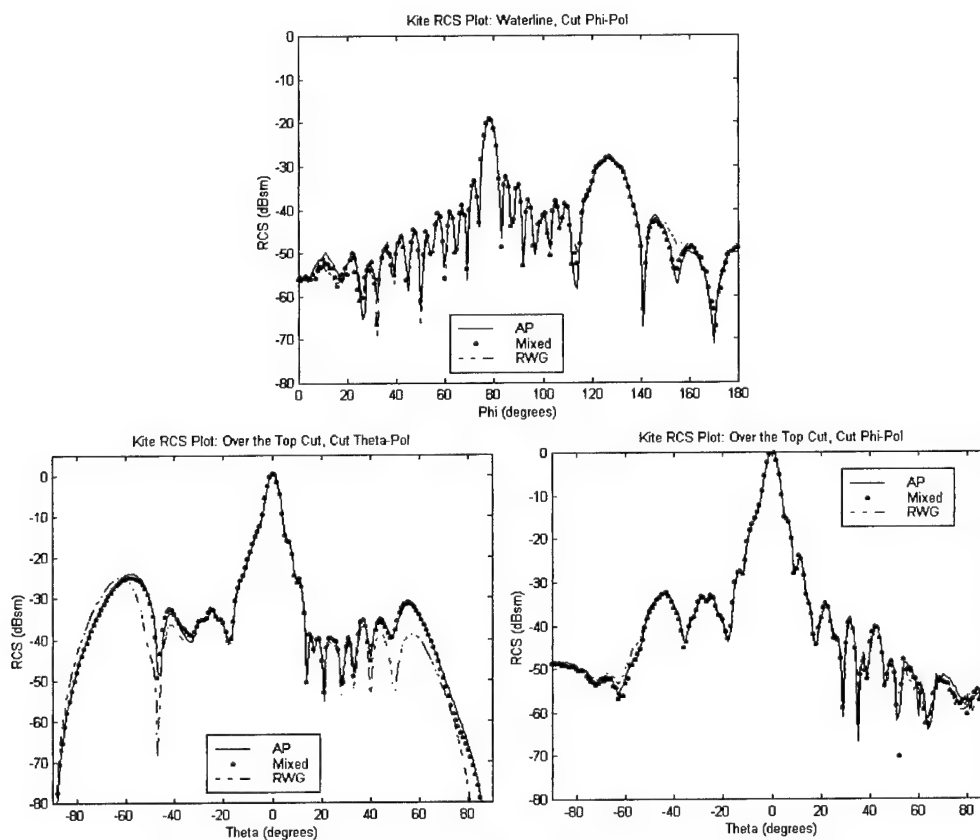
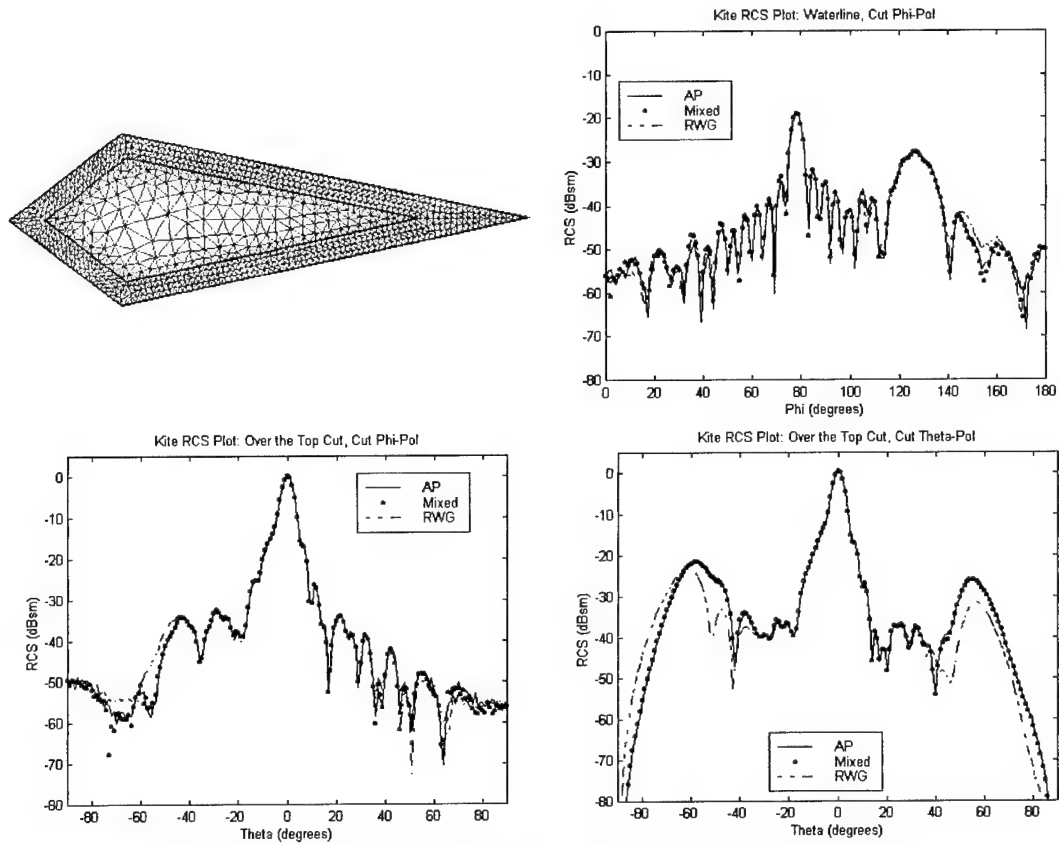


Figure 4.10: 10GHz Kite RCS Plot,  $d = 1.5\text{ cm}$ , Density Factor =  $12/3$



**Figure 4.11:** 10 GHz Kite RCS Plots,  $d = 1\text{ cm}$ , Mesh Density Factor = 12/3

Particularly visible in Figure 4.11, we see that the mixed basis function RCS curve closely matches the AP basis function curve even with  $d = 1\text{ cm}$ . The RWG curve does not match because the sampling rate over most of the kite is less than ten elements per wavelength. Remember that the mixed basis function method has a lower implementation cost than using all AP basis functions.

#### **Selection of the RWG Region Thickness:**

If we view the above RCS data plotted differently, we can consider the implications of changing  $d$ . Figure 4.12 shows RCS curves for mixed basis function implementation with  $d = 1\text{ cm}$ ,  $1.5\text{ cm}$ , and for a uniform mesh (12/12). This figure is included here

because it is the most interesting of the orientations. The other eight orientations are included in Appendix D. We can see that as  $d$  is decreased, the RCS values deviate from the highest sampling rate curve at certain theta angle ranges. Hence, we experience the traditional trade-off of number of unknowns verses quality of solution.

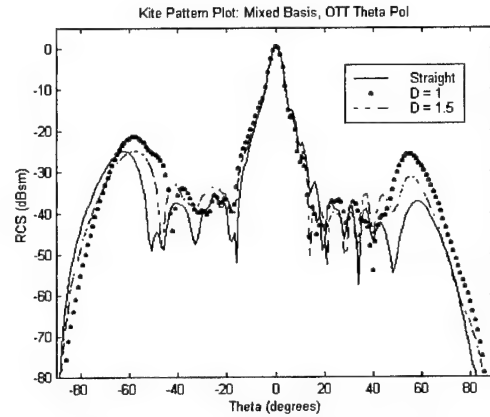


**Figure 4.12:** 10 GHz Kite RCS, OTT-T Mixed Basis Functions

### Convergence:

In numerical methods, rate of iterative solution convergence is a constant concern. Since AP elements in the matrix require computation at every incident angle, we are naturally concerned about the convergence of the matrix solution for each angle. Since we wanted a convergence measure relative to an all-RWG basis function implementation for a given mesh, we chose to observe the matrix condition number, the ratio of largest to smallest eigenvalue. Figure 4.13 shows that although the condition number varies with angle, there is no apparent correlation and the overall variation relative to RWG-only is minimal. Therefore, we can conclude that additional matrix convergence issues do not result from using combined basis functions.

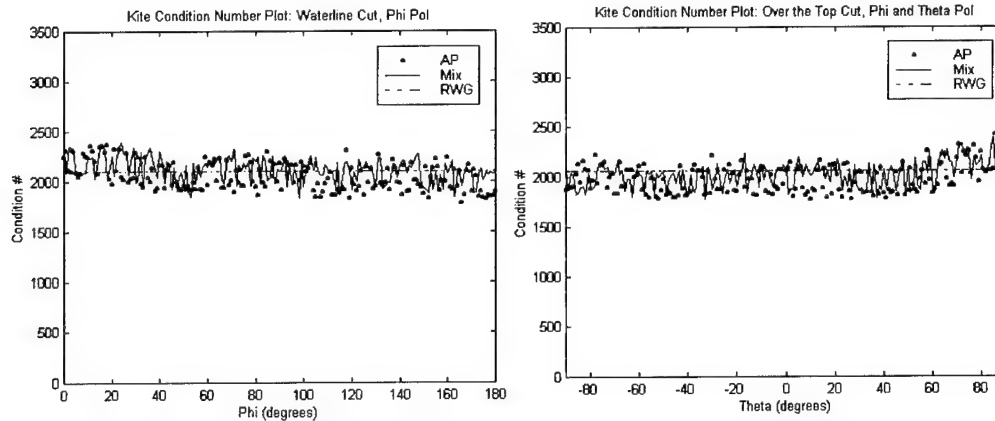


**Figure 4.13:** 10 GHz Kite,  $d = 1$  cm, Condition Number vs. Incident Angle

### Mesh Density Analysis:

We completed a mesh analysis to study two particular issues. First, how dense should the mesh be to provide a converged RCS value? Second, how sparse can the inner mesh be? Using 12 GHz, the number of unknowns necessary increases dramatically (33%) from the 10GHz case (table 4.1). However, the increased frequency allows more flexibility for this particular analysis. Half of a wavelength at 12 Ghz is approximately 1.25 cm so for the 12 GHz experiments we use  $d = 1.25$ . We considered the phi angle of 63 degrees on the OTT-T cut since this was the region of maximum discrepancy among RCS curves.

Addressing the second question above first, we find that due to physical meshing constraints, a 2.8 mesh density factor is the lowest possible. Below 2.8, the mesh has the same number of unknowns. That is, the kite is geometrically constricted below 2.8 mesh density factor.

Basis	Density	RCS	Cond #
RWG	14,14	-42.14	xxx.xx
RWG	12,12	-42.44	528.47
RWG	12,2.8	-31.76	2647.6
MIX	14,14	-41.40	577.48
MIX	12,12	-38.52	515.26
MIX	12,2.8	-31.22	3491.1

**Table 4.2:** Density Analysis  
 $\phi = 63^\circ$ ,  $\theta = 0^\circ$ , Freq = 12GHz



To answer our first

question, we again consider

$\theta = 0$  and  $\phi = 63$  since

this observation angle

appears to have the largest

RCS discrepancy. Using

RWG basis functions with a

density factor of 12/12, we

observe from table 4.2 that

the RCS value appears to

have converged since at a mesh density factor of 14/14 is very close to the value at 12/12.

Using mixed basis functions on a uniform mesh, the RCS value does not converge until a

mesh density of 14/14. RCS values for 12/12 and 12/2.8 are compared for mixed vs.

RWG basis functions in figure 4.14. Interestingly, the discrepancy in the  $\theta$  range of

discussion shows the RWG 12/12 value is most clearly matched by Mix 12/12 while

RWG 12/2.8 and Mix 12/2.8 match each

other, but not RWG 12/12. Aside from this

observation angle range, such discrepancy

does not arise (Appendix D). It appears

some other phenomenon may be affecting

our results in that observation angle range.

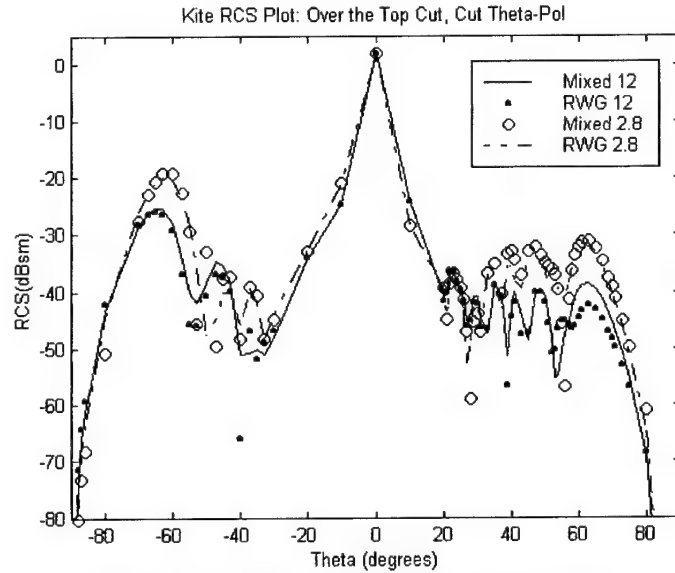


Figure 4.14: 12 GHz Kite RCS, OTT-T,  $d = 1.25\text{cm}$

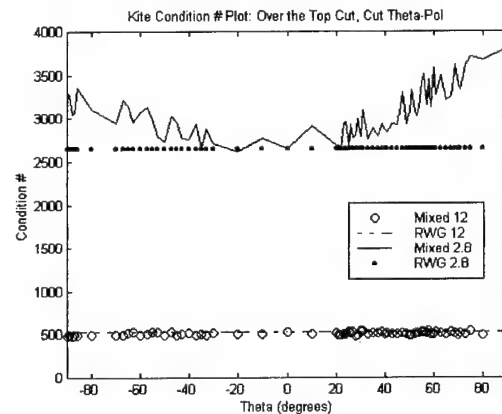


Figure 4.15: Condition Number vs. Incident Angle

One can see in Figure 4.15 that the condition numbers are much larger for 12/12 than for 12/2.8. This makes sense since the same problem is specified more finely in the 12/12 case. The angles studied are shown by the dots plotted in the RWG curve in Figure 4.15.

In the 12/2.8 mixed case, we see that we can maintain relatively accurate results (especially for theta angles near 0) for the kite using this methodology to reduce the number of unknowns.

#### 4. Extension to the EMCC Mini-Arrow

The kite can be extended to similar shape, in particular, the three-dimensional mini-arrow. The mini-arrow is formed by adding the point (8.935,0,3.932) to the kite and extending a line from each kite vertex to this new point. In figure 4.16 a tenth of a

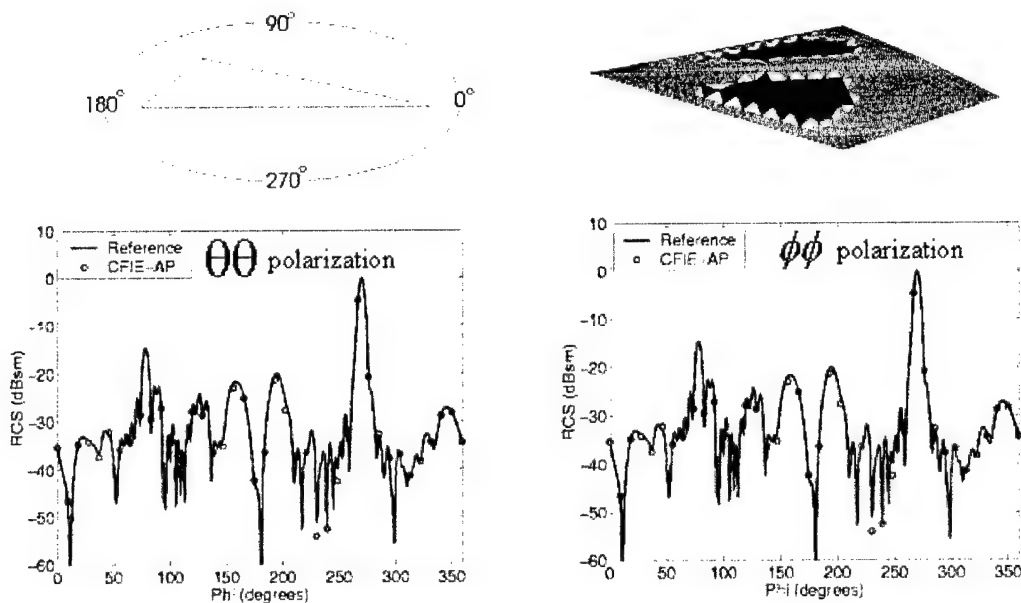


Figure 4.16: Mini-arrow scattering at 9 GHz.[3]

wavelength sampled RWG only mesh (reference) is compared with a graded mesh using the combined basis function methodology at 9 GHz. This demonstrates the method's ability to simulate three-dimensional objects using CFIE ( $\alpha = .5$ ) with mixed basis functions. CFIE-AP refers to the implementation of RWG and AP basis functions. It should be noted that UIUC [3] computed these results and duplication at MSU was deemed unnecessary. Next, we consider the mini-arrow at 12 GHz to determine edge reduction potential. However, due to the small surface area of each surface of the mini-arrow, the mesh is geometrically restricted rather than current restricted. We do not achieve a significant reduction in edge unknowns. Hence, the combined basis function methodology is only beneficial for large smooth sections.

## CHAPTER 5: CONCLUSION

We conclude with a summary of the research and the knowledge gained along with noting some particular challenges and future work.

### *1. Summary*

In the past, people have used Rao-Wilton-Glisson expansion and testing functions to solve the PEC scattering integral equation problem. For accurate results, this method requires element edge sizes at most a tenth of a wavelength or equivalently, approximately one hundred element edges per square wavelength. Thus, increases in frequency yield exponentially larger problems. Aberegg and Peterson [6] addressed the issue by multiplying the RWG function by the phase term of the incident field (i.e. asymptotic phase functions). While AP functions allow for less dense sampling in regions where the surface current phase is not rapidly changing, they require computing each matrix element at each angle of incidence, a costly disadvantage. Since AP functions still require high sampling rates near discontinuities, using RWG functions in those regions eliminates some of the added computation. Thus, the combination of RWG and AP basis and expansion functions on the same surface has the advantages of both methods. This research shows that such a combination of functions, appropriately used, does in fact achieve benefits of both, faster computation time from RWG, less unknowns from AP. We find that the gain is maximized for surfaces where the majority of the element edges (not necessarily the majority of the surface) use RWG functions. We have also shown that the advantages of the methodology are highly dependent on the physical characteristics of the geometry. Unique contributions from this research include:

1. Impedance matrix form shown in equation (2.22).
2. Use of the traditional singularity extraction technique [21] with asymptotic phase basis functions over flat triangles.
3. Convergence and mesh analysis for the kite geometry.
4. Investigation of region specific sampling with combined basis functions.

### **Summary of Results from Specific Geometries**

The kite and square geometries show approximately 35% and 68% (respectively) reduction in unknowns when discretized using a graded mesh and RWG-AP combination as compared to a tenth of a wavelength RWG-only meshing. With the number of AP elements minimized and their usage location chosen wisely, matrix element computation is significantly reduced from an all AP scheme. Therefore, for such geometries, the combination of basis and expansion functions is a more effective solution method than either AP or RWG used by alone.

For the mini-arrow geometry, we find that due to the small surface area of its side surfaces, the meshing is geometrically constricted. On such a geometry, the reduction of unknowns is not significant and the introduction of any AP elements to an RWG-only implementation actually increases the solution cost since matrix elements must be recomputed at each incident angle.

In a related effort in conjunctions with UIUC [3], we found that the conesphere geometry with  $C^2$  continuity across the sphere-cone interface can benefit from an AP only type solution. On the conesphere, the number of elements in the mesh away from the

discontinuity is kept large due to the curvature of the object. We found that the introduction of RWG elements near the discontinuity had minimal affect in reducing the design cost since the *number* of RWG tested and RWG expanded matrix element entries was small compared to the AP tested AP expanded entries, as shown in Figure 5.1. An AP-only solution method may be better than RWG-only; however, this depends on the memory and processor resources available (AP-only is more processor intensive while RWG-only requires more memory). Regardless, for the conesphere geometry a mixed implementation reduces overall costs some, but the geometry lends itself to an AP only mesh.

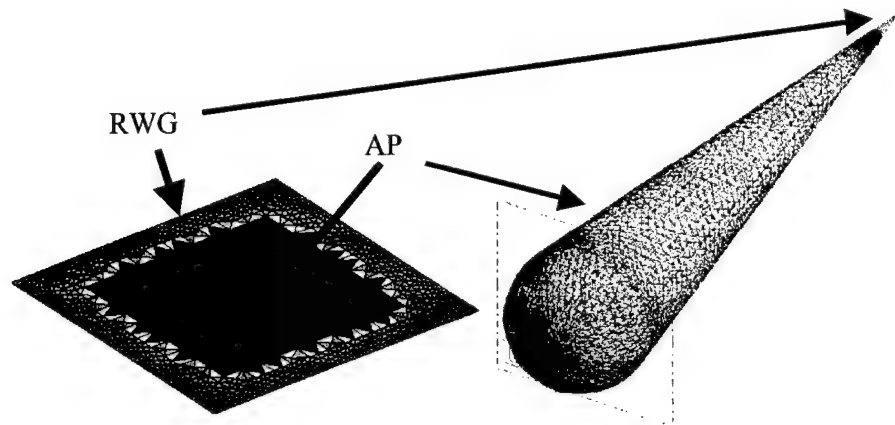


**Figure 5.1:** Graded Mesh on Square Plate vs. Conesphere

## Conclusion

For all the objects considered, the AP only and RWG-AP combination RCS values we observed were accurate relative to the traditional tenth of a wavelength sampled, RWG tested, RWG expanded method of moments numerical solution. On large, smooth surfaces with low curvature the RWG-AP combined basis and testing function method is a more effective solution than solely an RWG or AP implementation.

## ***2. Challenges***

- The usual long run times inherent in most numerical methods always have an impact on the number of different implementations one can study. Several simple and electrically small objects were considered in this research to quickly gain some insight into the fundamental characteristics of each methodology. From this information, we can begin to estimate how each might work on more numerically intensive problems. As computational resources continue to become more powerful with time, we can broaden the scope of our studies.
- Discretizing an object into a consistently “good” mesh is a particularly difficult task. It is an art form in itself, but is essential to quality numerical results. Since the scattering problem is sensitive to discontinuities, a mesh that accurately describes a testing object is crucial to attempting measured comparisons. Both high quality meshing programs (e.g. SDRC IDEAS, PRO-ENGINEER, etc.) and a highly talented mesh generation engineer are required to obtain high quality meshes.
- The essential difficulty with the method of moments matrix solution is the requirement for large amounts of computer RAM. As frequency increases, so does the need for memory.

## ***3. Future Work***

Following this research it would be beneficial to study this method with more objects and at higher frequencies to broaden the knowledge base and understanding of the practicality of the combined basis function method. Specifically, extended studies with curved

surfaces using six-point second order triangles have been presented in [3] and further research would be very beneficial.

From a more general perspective, the possibility for other basis functions with the method of moments has the potential to dramatically improve the scattering problem. Further application of the fast multipole method [3] can impact the solution cost for large matrices.

It would be of particular interest to consider applying the AP method to radiation studies since antenna problems involve only one right hand side of the integral equation. Thus, the advantages of AP might be realized without the disadvantage of needing to compute the matrix elements for multiple incidence angles.



## **APPENDICES**

## APPENDIX A: FUNDAMENTAL THEORY

There are three sections to this fundamental electromagnetics theory appendix. We begin with the independent large-scale form of Maxwell's equations, the fundamental starting point for electromagnetics theory, and almost all electrical physics for that matter. The vector potential quantities are then developed and finally a brief discussion of the Green's function as implemented in the above research. These are included in an attempt at completeness. Since we very well could have started with the results this development derives, these basic concepts are included as an appendix. Hopefully their inclusion will enable those not familiar with the electromagnetics discipline to understand and critically evaluate the fundamental challenges faced when we apply the theory to real situations.

### *1. Maxwell's Equations*

Definitions: (All the following quantities are functions of time and a spatial position vector  $\mathbf{r}$ .)

$\mathbf{E}$  = electrical field intensity (Volts)

$\mathbf{B}$  = magnetic flux density

$\mathbf{H}$  = magnetic field intensity

$\mathbf{D}$  = electric flux density

$\mathbf{J}$  = moving charge density (Amperes per square meter)

$\rho$  = charge density (Coulomb's per cubic meter)

Constants:

$$\epsilon_0 = \frac{1}{36\pi} * 10^{-9} \text{ Farads per meter} \quad \dots \text{permittivity of free space}$$

$$\mu_0 = 4\pi * 10^{-7} \text{ Henry's per meter} \quad \dots \text{permeability of free space}$$

Parameters of a medium:

$$\epsilon = \epsilon_r \epsilon_0 \quad \text{describes the permittivity in relation to free space and}$$

$$\mu = \mu_r \mu_0 \quad \text{describes the permeability relative to free space while}$$

$$\sigma \quad \text{describes the conductivity of a medium.}$$

In general, S is any open surface bounded by a closed contour C. Therefore, our fundamental independent Maxwell's equations include Faraday's (A.1) and Ampere's laws (A.2).

$$\oint_c \mathbf{E} \cdot d\mathbf{l} = -\frac{d}{dt} \int_s \hat{n} \cdot \mathbf{B} ds \quad \dots \text{Faraday's law} \quad (\text{A.1})$$

$$\frac{1}{\mu_0} \oint_c \mathbf{B} \cdot d\mathbf{l} = \epsilon_0 \frac{d}{dt} \int_s \hat{n} \cdot \mathbf{E} ds + \int_s \hat{n} \cdot \mathbf{J} ds \quad \dots \text{Ampere's law} \quad (\text{A.2})$$

Conservation of electrical charge requires

$$\int_s \hat{n} \cdot \mathbf{J} ds = -\frac{d}{dt} \int_v \rho dt. \quad (\text{A.3})$$

Equations (A.1)-(A.3) are in large-scale form. Assuming that C and S are not functions of time, we can pull the time derivative inside the surface integral. Applying Stoke's

Theorem,  $\int_s \nabla \times \mathbf{V} \cdot \hat{n} ds = \oint_c \mathbf{V} \cdot d\mathbf{l}$ , to the left hand side of (A.1) and moving the right

hand side of (A.1) to the left we get  $\int_s \left[ \nabla \times \mathbf{E} + \frac{d}{dt} \mathbf{B} \right] \cdot \hat{n} ds = 0$ . Since this holds for any surface, the bracketed quantity = 0 or equivalently,

$$\nabla \times \mathbf{E} = -\frac{d}{dt} \mathbf{B} \quad (\text{A.4})$$

If we apply Stoke's Theorem to the left of (A.2), move the right hand side to the left and combine the integrals, we can use the same argument as above (equation is true for any S) to get,

$$\frac{1}{\mu_o} \nabla \times \mathbf{B} = \mathbf{J} + \epsilon_o \frac{d}{dt} \mathbf{E} \quad (\text{A.5})$$

If we apply the Divergence Theorem,  $\int_v \nabla \cdot \mathbf{V} dv = \oint_s \mathbf{V} \cdot \hat{n} ds$ , to the left hand side of the constraint equation, combine the integrals, and note that it holds for all volumes  $v$ , we get,

$$\nabla \cdot \mathbf{J} = -\frac{d}{dt} \rho \quad (\text{A.6})$$

Equations (A.4)-(A.6) are the point form of the independent Maxwell equations. If we take the divergence of both sides of (A.4), use the vector identity  $\nabla \cdot \nabla \times \mathbf{A} = 0$ , and invoke causality, we observe

$$\nabla \cdot \mathbf{B} = 0 \quad (\text{A.7})$$

Taking the divergence of both sides of (A.5), and use the same vector identity to get

$$\frac{d}{dt} \rho = \epsilon_o \frac{d}{dt} \nabla \cdot \mathbf{E} \Rightarrow \frac{d}{dt} [\epsilon_o \nabla \cdot \mathbf{E} - \rho] = 0 .$$

Time integrate both sides and invoke causality to get the point form of Gauss' law.

$$\nabla \cdot \mathbf{E} = \frac{\rho}{\epsilon_o} \quad (\text{A.8})$$

In general media (not necessarily free space), we define auxiliary equations to include non-zero magnetization  $\mathbf{M}$  and polarization  $\mathbf{P}$ , also functions of time and space.

$$\mathbf{H} = \frac{1}{\mu_o} \mathbf{B} - \mathbf{M} \text{ (Amperes per meter)} \quad \dots \text{magnetic field intensity}$$

$$\mathbf{J} = \mathbf{J}^i + \sigma \mathbf{E} \text{ (Amperes per square meter)} \quad \dots \text{total free current}$$

$$\mathbf{D} = \epsilon_o \mathbf{E} + \mathbf{P} \text{ (Coulombs per meter)} \quad \dots \text{electric induction, flux density}$$

In simple (linear, isotropic) media, we then define  $\mathbf{P}$  and  $\mathbf{M}$  in terms polarization

susceptibility  $\chi_c$  and magnetization susceptibility  $\chi_m$ .  $\mathbf{P} = \epsilon_o \chi_c \mathbf{E}$  and  $\mathbf{M} = \chi_m \mathbf{H}$ . So by

substitution

$$\therefore \mathbf{D} = \epsilon_o \mathbf{E} + \mathbf{P} = \epsilon_o \mathbf{E} + \epsilon_o \chi_c \mathbf{E} = \epsilon_o (1 + \chi_c) \mathbf{E} = \epsilon(\mathbf{r}) \mathbf{E} = \epsilon_o \epsilon_r(\mathbf{r}) \mathbf{E} \text{ and}$$

$$\mathbf{B} = \mu_o (\mathbf{H} + \mathbf{M}) = \mu_o (1 + \chi_m) \mathbf{H} = \mu(\mathbf{r}) \mathbf{H} = \mu_o \mu_r(\mathbf{r}) \mathbf{H}$$

The above equations are valid even for inhomogeneous media. By substitution into (A.4)

and (A.5),  $\nabla \times \mathbf{E} = -\frac{d}{dt} \mu(\mathbf{r}) \mathbf{H}$  and  $\frac{1}{\mu_o} \nabla \times \mu(\mathbf{r}) \mathbf{H} = \mathbf{J} + \frac{d}{dt} \mathbf{D}$ . If we assume the

media is *homogeneous* (permeability and permittivity are not functions of space),  $\epsilon$  and  $\mu$

can come out of the derivatives, leaving

$$\nabla \times \mathbf{E} = -\mu \frac{d}{dt} \mathbf{H}, \quad (\text{A.9})$$

$$\nabla \times \mathbf{H} = \mathbf{J} + \frac{d}{dt} \mathbf{D}. \quad (\text{A.10})$$

For use in the frequency domain, it is useful to define phaser notation for the vector field

quantities. We can write  $\mathbf{E}(\mathbf{r}, t) = \mathbf{E}_o(\mathbf{r}) \cos(\omega t + \phi_E(\mathbf{r}))$  where  $\omega = 2\pi f$ . Using Euler's

equation to expand the cosine function into exponentials and considering the real part, the

following is equivalent,

$$\mathbf{E}(\mathbf{r}, t) = \mathbf{E}_o(\mathbf{r}) \operatorname{Re} \left\{ e^{j(\omega t + \phi_E(\mathbf{r}))} \right\} = \operatorname{Re} \left\{ \mathbf{E}(\mathbf{r}) e^{j\phi_E(\mathbf{r})} e^{j\omega t} \right\}. \quad (\text{A.11})$$

We now make the following key observations:

1. All the vector field parameters can be written using a similar argument as for the electric field.
2. The operator  $\mathbf{Re}\{ \}$  commutes with addition, subtraction, integration, and differentiation.
3. Time integration transforms to multiplication by  $j\omega$  in the frequency domain.
4. Since every parameter contains an  $e^{j\omega t}$  term, we can suppress it for notational purposes.

The resulting time harmonic Maxwell Equations and the continuity equation, with vector field quantities having spatial dependence and a suppressed  $e^{j\omega t}$  term are:

$$\nabla \times \mathbf{E} = -j\omega\mu\mathbf{H} \quad (\text{A.12})$$

$$\nabla \times \mathbf{H} = \mathbf{J} + j\omega\mu\mathbf{E} = \mathbf{J}^i + (\sigma + j\omega\epsilon)\mathbf{E} \quad (\text{A.13})$$

$$\nabla \cdot \mathbf{E} = \frac{1}{\epsilon} \rho(\mathbf{r}) \quad (\text{A.14})$$

$$\nabla \cdot \mathbf{H} = 0 \quad (\text{A.15})$$

$$\nabla \cdot \mathbf{J} = j\omega\rho(\mathbf{r}) \quad (\text{A.16})$$

Notes:

- To convert to the time domain, unsuppress the  $e^{j\omega t}$  term and take the real part.
- The above form of the equations is under the relatively strong assumption of *linear, homogeneous, isotropic* media.
- If the medium is free space,  $\epsilon = \epsilon_0$ ,  $\mu = \mu_0$ ,  $\sigma = 0$ . If source free,  $\mathbf{J}^i = 0$ .

## 2. Boundary Conditions

For a comprehensive explanation of boundary conditions, see [9], page 13. A summary is stated here.

At the interface of two media with differing electrical properties, Maxwell's equations dictate the following:

- The tangential components of the electric field across an interface between two media with no impressed magnetic current densities along the boundary of the interface are continuous.

$$\hat{n} \times (\mathbf{E}_2 - \mathbf{E}_1) = 0 \quad (\text{A.17})$$

- The tangential components of the magnetic field across an interface, along which there exists a surface current density  $\mathbf{J}_s$  (A/m) are discontinuous by an amount equal to the electric current density.

$$\hat{n} \times (\mathbf{H}_2 - \mathbf{H}_1) = \mathbf{J}_s \quad (\text{A.18})$$

In a medium with infinite conductivity, the tangential components of  $\mathbf{E}$  and  $\mathbf{H} = 0$ . Thus on the surface of a perfect electrical conductor (PEC), the tangential component of the total electric field equals zero and the tangential component of the total magnetic field is equal to the surface current density.

## 3. Vector Potentials

By making a change of variables, we can represent the electric and magnetic fields in terms of intermediate variables, the electric and magnetic vector potentials. Using the Lorentz gauge condition, we can manipulate the equations into a standard differential

equation with solutions. In this section, we will define the vector potentials and derive the scalar Helmholtz equation.

### **Magnetic Vector Potential:**

Since we know  $\nabla \cdot \mu \mathbf{H} = 0$  and the vector identity  $\nabla \cdot (\nabla \times \mathbf{V}) = 0$ , define  $\mathbf{A}$  such that

$$\mu \mathbf{H} = \nabla \times \mathbf{A}. \quad (\text{A.19})$$

By substitution into (A.12),

$$\nabla \times \mathbf{E} = -j\omega(\nabla \times \mathbf{A}) \Rightarrow \nabla \times (\mathbf{E} + j\omega \mathbf{A}) = 0 \quad (\text{A.20})$$

Since we have the vector identity  $\nabla \times (-\nabla \mathbf{V}) = 0$ , define  $\Phi_e$  such that

$$\mathbf{E} = -\nabla \Phi_e - j\omega \mathbf{A}. \quad (\text{A.21})$$

Substitute (A.19) and (A.21) into (A.13),

$$\nabla \times \left( \frac{\nabla \times \mathbf{A}}{\mu} \right) = \mathbf{J}^i + (\sigma + j\omega\epsilon)(-\nabla \Phi_e - j\omega \mathbf{A}). \quad (\text{A.22})$$

By homogeneity, can factor  $\frac{1}{\mu}$  out of the left hand side and multiply (A.22) by  $\mu$ .

Define the wave number  $k$  such that  $k^2 = -j\omega\mu(\sigma + j\omega\epsilon)$ . Then (A.22) becomes

$$\nabla \times \nabla \times \mathbf{A} = \mathbf{J}^i - \mu(\sigma + j\omega\epsilon)\nabla \Phi_e + k^2 \mathbf{A}. \quad (\text{A.23})$$

Using the Lorentz gauge condition,

$$\Phi_e = \frac{j\omega}{k^2} \nabla \cdot \mathbf{A}, \quad (\text{A.24})$$

and the vector identity  $\nabla \times \nabla \times \mathbf{V} = \nabla(\nabla \cdot \mathbf{V}) - \nabla^2 \mathbf{V}$ , we can write (A.23) as



$$\nabla^2 \mathbf{A} + k^2 \mathbf{A} = -\mu \mathbf{J}^i. \quad (\text{A.25})$$

**Electric Vector Potential:** (source free space.)

Using similar steps as above, since  $\nabla \cdot \mathbf{E} = 0$ , define  $\mathbf{F}$  such that

$$\mathbf{E} = -\nabla \times \mathbf{F}. \quad (\text{A.26})$$

Then by substitution into (A.13),

$$\nabla \times \mathbf{H} = \mathbf{J} + j\omega\mu(-\nabla \times \mathbf{F}) \Rightarrow \nabla \times (\mathbf{H} + j\omega\epsilon\mathbf{F}) = 0. \quad (\text{A.27})$$

We can then define  $-\nabla\Phi_m \ni \mathbf{H} = -\nabla\Phi_m - j\omega\mu\mathbf{F}$ . Using the same vector identities and substituting into (A.12),

$$\nabla \times \nabla \times \mathbf{F} = j\omega\mu(-\nabla\Phi_m - j\omega\mu\mathbf{F}). \quad (\text{A.28})$$

By choosing the Lorentz gauge condition again,  $\Phi_m = \frac{j\omega\epsilon}{k^2} \nabla \cdot \mathbf{F}$  and the same vector identity as above, we can write (A.28) as

$$\nabla^2 \mathbf{F} + k^2 \mathbf{F} = 0. \quad (\text{A.29})$$

Recall that  $\mathbf{A}, \mathbf{F}, \mathbf{E}, \mathbf{H}, \Phi_{e,m}$ , and  $s$  are all functions of position.

#### ***4. Scalar Green's Function***

Let us consider the scalar Helmholtz equation from section 2 of this appendix,

$$\nabla^2 \psi(\mathbf{r}) + k^2 \psi(\mathbf{r}) = -s(\mathbf{r}). \quad (\text{A.30})$$

Recall from above that  $\psi$  is the unknown wave function,  $s(\mathbf{r})$  is a known volume source density, and  $k$  is the wave number. For a single point source  $\mathbf{r}'$  observed at  $\mathbf{r}$ ,  $s(\mathbf{r}) = \delta(\mathbf{r} - \mathbf{r}')$ , we define the

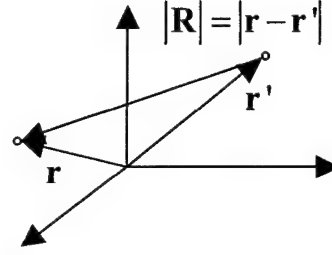


Figure A.1: Position Vectors

Green's function,  $g(\mathbf{r}|\mathbf{r}')$ , as the field at any  $\mathbf{r}$  due to

$\mathbf{r}'$ . Thus the Green's function for the scalar Helmholtz equation is

$$\nabla^2 g(\mathbf{r}|\mathbf{r}') + k^2 g(\mathbf{r}|\mathbf{r}') = -\delta(\mathbf{r} - \mathbf{r}'). \quad (\text{A.31})$$

(A.31) can be solved using the integral transform technique.

First, take the Fourier transform.

$$-(\lambda_x^2 + \lambda_y^2 + \lambda_z^2) \tilde{g}(\boldsymbol{\lambda}|\mathbf{r}') + k^2 \tilde{g}(\boldsymbol{\lambda}|\mathbf{r}') = -e^{-j\boldsymbol{\lambda} \cdot \mathbf{r}'} \quad (\text{A.32})$$

Then solve for  $\tilde{g}$ .

$$\tilde{g}(\boldsymbol{\lambda}|\mathbf{r}') = \frac{e^{-j\boldsymbol{\lambda} \cdot \mathbf{r}'}}{(\lambda^2 - k^2)} = \frac{e^{-j\boldsymbol{\lambda} \cdot \mathbf{r}'}}{(\lambda - k)(\lambda + k)} \quad (\text{A.33})$$

Then, take the inverse Fourier transform.

$$g(\mathbf{r}|\mathbf{r}') = \frac{1}{(2\pi)^3} \int_{-\infty}^{\infty} \int_{-\infty}^{\infty} \int_{-\infty}^{\infty} \tilde{g}(\boldsymbol{\lambda}, \mathbf{r}') e^{-j\boldsymbol{\lambda} \cdot \mathbf{r}} d^3\boldsymbol{\lambda} \quad (\text{A.34})$$

To analytically evaluate the above integral (which has poles at  $\pm k = \lambda$ ), switch to polar  $\lambda$ -space, evaluate over a pole excluding contour in the upper and lower half planes exploiting Cauchy's Integral Theorem resulting in

$$g(\mathbf{r}|\mathbf{r}') = \frac{1}{4\pi R} e^{-jkR} \text{ where } R = |\mathbf{r} - \mathbf{r}'|. \quad (\text{A.35})$$

Since  $g(\mathbf{r}|\mathbf{r}')$  is the point source solution and  $\mathbf{J}(\mathbf{r}')$  includes the magnitude and distribution throughout a source region, by superposition,

$$\mathbf{A} = \mu \int_V \mathbf{J}(\mathbf{r}') g(\mathbf{r} | \mathbf{r}') dV' \quad (\text{A.36})$$

is a solution to (A.25). For a surface current density, (A.36) reduces to

$$\mathbf{A} = \mu \int_s \mathbf{J}(\mathbf{r}') g(\mathbf{r} | \mathbf{r}') ds', \quad (\text{A.37})$$

and is valid for open and closed s.

## APPENDIX B: VECTOR IDENTITIES

$\mathbf{V}$  is a vector function;  $w$  is a scalar function.

$$\nabla \cdot (\nabla \times \mathbf{V}) = 0 \quad (\text{B.1})$$

$$\nabla \times (-\nabla V) = 0 \quad (\text{B.2})$$

$$\nabla \times \nabla \times \mathbf{V} - \nabla \nabla \cdot \mathbf{V} = \nabla^2 \mathbf{V} \quad (\text{B.3})$$

$$\nabla \cdot (w \mathbf{V}) = w \nabla \cdot \mathbf{V} + \mathbf{V} \cdot \nabla w \quad (\text{B.4})$$

$$\nabla \times (\mathbf{V} w) = w \nabla \times \mathbf{V} - \mathbf{V} \times \nabla w \quad (\text{B.5})$$

## APPENDIX C: INNER KITE VERTICES

The following is the calculation as input to the SkyMesh2™ file. Based on the known outer vertices and the desired out region thickness, using geometry, this calculates the inner triangle vertices.

```
# Kite Definition (x-z plane)
k1x = 0
k1y = 0
k1z = 0
k2x = 5.05
k2y = 3.85
k2z = 0
k3x = 23.495
k3y = 0
k3z = 0
k4x = 5.05
k4y = -3.85
k4z = 0

#Calculation of inner kite based on d and outer kite
M1 = (k2y-k1y)/(k2x-k1x)
M2 = (k3y-k2y)/(k3x-k2x)
M3 = (k4y-k3y)/(k4x-k3x)
M4 = (k1y-k4y)/(k1x-k4x)

x1 = (k2x+k1x)/2+d*(k2y-k1y)/sqrt((k2y - k1y)^2 + (k2x - k1x)^2)
x2 = (k3x+k2x)/2+d*(k3y-k2y)/sqrt((k3y - k2y)^2 + (k3x - k2x)^2)
x3 = (k4x+k3x)/2+d*(k4y-k3y)/sqrt((k4y - k3y)^2 + (k4x - k3x)^2)
x4 = (k1x+k4x)/2+d*(k1y-k4y)/sqrt((k1y - k4y)^2 + (k1x - k4x)^2)

y1 = (k2y+k1y)/2+(k2x+k1x-2*x1)/(2*M1)
y2 = (k3y+k2y)/2+(k3x+k2x-2*x2)/(2*M2)
y3 = (k4y+k3y)/2+(k4x+k3x-2*x3)/(2*M3)
y4 = (k1y+k4y)/2+(k1x+k4x-2*x4)/(2*M4)

z1 = (M4*x4+y1-M1*x1-y4)/(M4-M1)
z2 = (M1*x1+y2-M2*x2-y1)/(M1-M2)
z3 = (M2*x2+y3-M3*x3-y2)/(M2-M3)

w2 = M2*z2-M2*x2+y2
w4 = -w2

# Outer Kite
1      k1x    k1y    k1z
2      k2x    k2y    k2z
3      k3x    k3y    k3z
4      k4x    k4y    k4z

# Inner kite
5      z1      0.0    0.0
6      z2      w2      0.0
7      z3      0.0    0.0
8      z2      w4      0.0
```

## APPENDIX D: ADDITIONAL KITE SEPARATION COMPARISONS

The following sets of images are in addition to the discussion in Chapter 4.3: RWG Region thickness for the kite.

Figure D.1 shows the AP results comparing different thicknesses of the RWG region. The AP-WL-P and AP-OTT-P plots show close matching for all three thicknesses. The AP-OTT-T plot is comparable to the MIX-OTT-T plot discussed in Chapter 4.3. Figure D.2 shows closely matched RCS curves for the MIX-OTT-P and MIX-WL-P cuts. Figure D.3 again shows closely matched RCS curves for the RWG only case. Refer to Chapter 4.3 for further discussion.

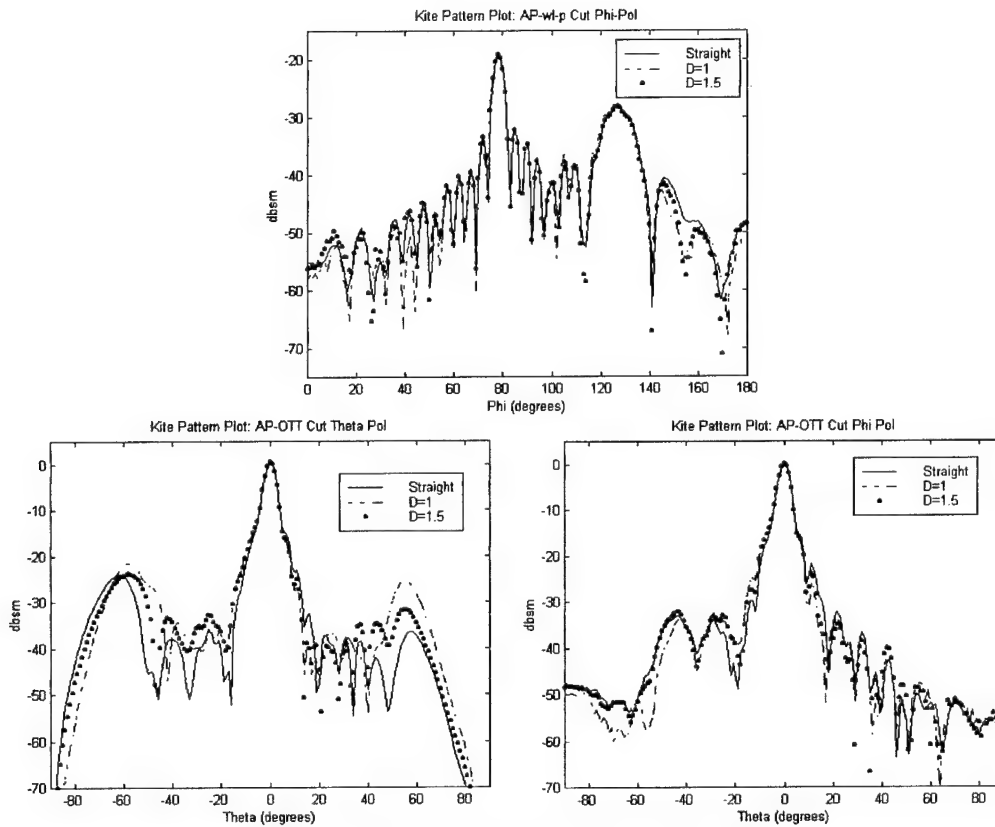
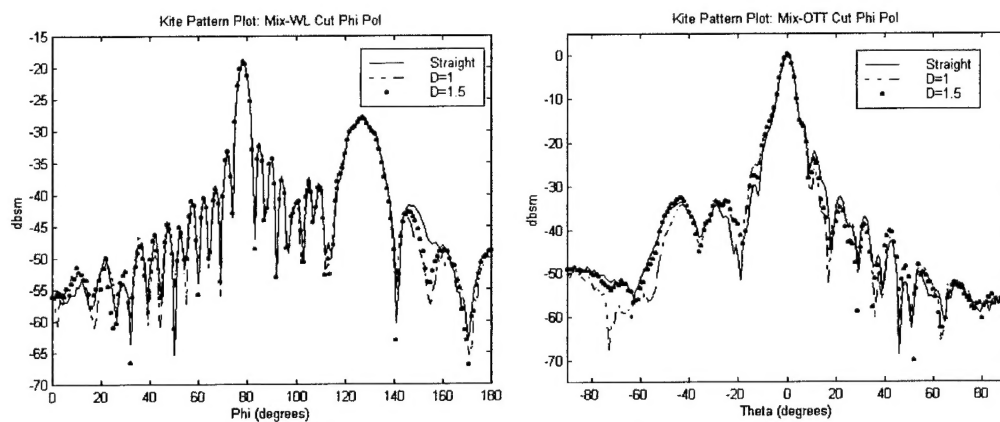
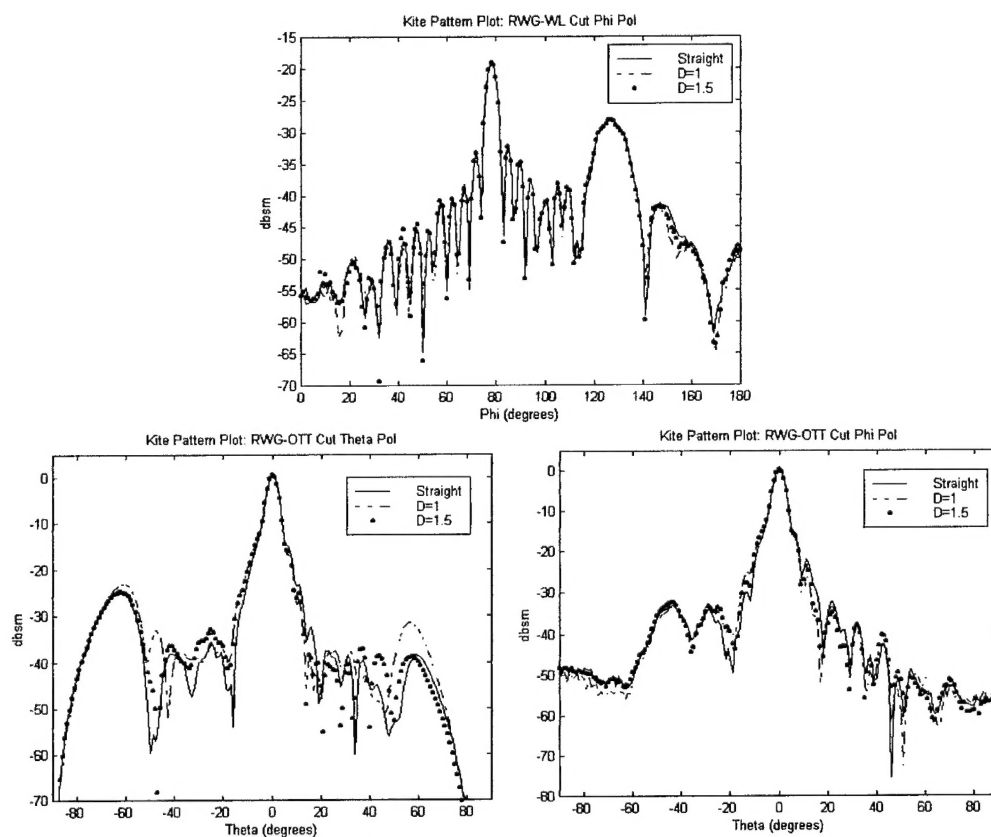


Figure D.1: 10 GHz Kite RCS, AP Basis Functions



**Figure D.2: 10 GHz Kite RCS, Mixed Basis Functions**



**Figure D.3: 10 GHz Kite RCS, RWG Basis Functions**

## **BIBLIOGRAPHY**



## BIBLIOGRAPHY

- [1] S. Rao, D. R. Wilton, and A. W. Glisson, "Electromagnetic Scattering by Surfaces of Arbitrary Shape," *IEEE Trans. Antenna Propagat.*, p. 409, May 1982.
- [2] K. R. Aberegg, Electromagnetic Scattering Using the Integral Equation-Asymptotic Phase Method, Ph.D. Dissertation, Georgia Inst. of Tech., Nov. 1995.
- [3] M. A. Kowolski et al, "On the Three-Dimensional Integral-Equation Asymptotic Phase (IE-AP) Method," *PIERS*, p. 136, 2000.
- [4] R. F. Harrington, Time-Harmonic Electromagnetic Fields, McGraw Hill, 1961.
- [5] R. E. Collin, Field Theory of Guided Waves, 2nd Ed., IEEE Press, p. 142, 1991.
- [6] K. R. Aberegg, A. F. Peterson, "Application of the Integral Equation - Asymptotic Phase Method to Two-Dimensional Scattering," *IEEE Trans. Antenna Propagat.*, p. 534-537, May 1995.
- [7] D. R. Wilton et al, "Potential Integrals for Uniform and Linear Source Distributions on Polygonal and Polyhedral Domains," *IEEE Trans. Antenna Propagat.*, p. 276, March 1984.
- [8] P. R. Haddad, "Scattering by Non-Planar Surfaces," University of Michigan, 1991.
- [9] C. A. Balanis, Advanced Engineering Electromagnetics, Wiley, 1989.
- [10] J. Mathews, R. Walker, Mathematical Methods of Physics, W.A. Benjamin, 1964.
- [11] K. M. Mitzner, "Numerical solution of the exterior scattering problem at eigenfrequencies of the interior problem," *Digest of the 1968 URSI Radio Science Meeting*, Boston, MA, International Union of Radio Scientists (URSI), p. 75, Sept. 1968. This conference digest not formally available from URSI.
- [12] J. R. Mautz and R. F. Harrington, "H-field, E-field, and combined-field solutions for conducting bodies of revolution," *Archiv für Elektronik und Übertragungstechnik (A. E. U.)*, vol. 32, pp. 157-163, 1978.
- [13] A. F. Peterson, S. L. Ray, and R Mittra, Computational Methods for Electromagnetics, IEEE Press, 1998.
- [14] J. L. Volakis and L. C. Kempel, "Electromagnetics: Computational Methods and Considerations," *IEEE Computational Science & Engineering*, p42, Spring, 1995.
- [15] J. J. H. Wang, Generalized Moment Method in Electromagnetics, Wiley-Interscience, 1991.

- [16] R. F. Harrington, Field Computations by Moment Method in Electromagnetics, Krieger, Malabar, Fla., 1982. [Reprint of original Macmillan ed., now reissued by IEEE Press, 1993.]
- [17] K. R. Aberegg, A. Taguchi, and A. F. Peterson, "Application of higher-order vector basis functions to surface integral formulations," *Radio Sci.*, vol. 31, pp. 1207-1213, 1996.
- [18] S. Caorsi, D. Moreno, and F. Sidoti, "Theoretical and numerical treatment of surface integrals involving the free-space Green's function," *IEEE Trans. Antenna Propagat.*, vol. 41, pp. 1296-1301, Sept. 1993.
- [19] E. J. Rothwell, M. J. Cloud, Electromagnetics, CRC Press LLC, 2001
- [20] D. P. Nyquist, "Advanced Electromagnetic Fields and Waves I: Class Notes", Michigan State University, 2000
- [21] D. R. Wilton, S. M. Rao, and A. W. Glisson, "Potential Integrals for Uniform and Linear Source Distributions on Polygonal and Polyhedral Domains," *IEEE Trans. Antenna Propagat.*, p. 276, March 1984.